Tellus SERIES B CHEMICAL AND PHYSICAL METEOROLOGY
PUBLISHED BY THE INTERNATIONAL METEOROLOGICAL INSTITUTE IN STOCKHOLM

Tellus (2009), 61B, 96–117

TELLUS

Airborne measurements of dust layer properties, particle size distribution and mixing state of Saharan dust during SAMUM 2006

By BERNADETT WEINZIERL[1,*], ANDREAS PETZOLD[1], MICHAEL ESSELBORN[1], MARTIN WIRTH[1], KATHARINA RASP[1], KONRAD KANDLER[2], LOTHAR SCHÜTZ[3], PETER KOEPKE[4] and MARKUS FIEBIG[5], [1]*Deutsches Zentrum für Luft- und Raumfahrt, Institut für Physik der Atmosphäre, Oberpfaffenhofen, 82234 Wessling, Germany;* [2]*Institut für Angewandte Geowissenschaften, Technische Universität Darmstadt, 64287 Darmstadt, Germany;* [3]*Institut für Physik der Atmosphäre, Johannes-Gutenberg-Universität Mainz, 55099 Mainz, Germany;* [4]*Meteorologisches Institut, Ludwig-Maximilians-Universität, 80333 München, Germany;* [5]*Department for Atmospheric and Climate Research, Norwegian Institute for Air Research (NILU), 2027 Kjeller, Norway*

(Manuscript received 2 January 2008; in final form 14 August 2008)

ABSTRACT

The Saharan Mineral Dust Experiment (SAMUM) was conducted in May/June 2006 in southern Morocco. As part of SAMUM, airborne in situ measurements of the particle size distribution in the diameter range 4 nm $< D_p <$ 100 μm were conducted. The aerosol mixing state was determined below $D_p <$ 2.5 μm. Furthermore, the vertical structure of the dust layers was investigated with a nadir-looking high spectral resolution lidar (HSRL). The desert dust aerosol exhibited two size regimes of different mixing states: below 0.5 μm, the particles had a non-volatile core and a volatile coating; larger particles above 0.5 μm consisted of non-volatile components and contained light absorbing material. In all cases, particles larger than 10 μm were present, and in 80% of the measurements no particles larger than 40 μm were present. The abundance of large particles showed almost no height dependence. The effective diameter D_{eff} in the dust plumes investigated showed two main ranges: the first range of D_{eff} peaked around 5 μm and the second range of D_{eff} around 8 μm. The two ranges of D_{eff} suggest that it may be inadequate to use one average effective diameter or one parametrization for a typical dust size distribution.

1. Introduction

The Saharan desert covers an area of about 9 million km^2 and is the largest desert on Earth, contributing to about 50–70% (Mahowald et al., 2005) of the annual global dust emissions. Dust storms are a significant source of coarse mode particles (e.g. Schütz and Jaenicke, 1974; Schütz and Jaenicke, 1978; d'Almeida and Schütz, 1983; de Reus et al., 2000). Mineral dust particles scatter and partly absorb solar radiation. Moreover, dust particles have the potential to alter the outgoing terrestrial radiation flux due to their large sizes (e.g. Haywood et al., 2005). The sign of the top of atmosphere radiative forcing of mineral dust aerosol is uncertain, in view of the competing nature of the negative solar radiative forcing and the positive terrestrial radiative forcing (e.g. Haywood and Boucher, 2000; IPCC, 2001). The presence of dust alters atmospheric heating rates, impacts on the hydrological cycle (e.g. Rosenfeld et al., 2001; Miller et al., 2004) and the formation of ice clouds (e.g. Ansmann et al., 2005). The spatial and temporal distribution of the radiative properties of dust are poorly understood over many regions of the world (e.g. Moorthy et al., 2007). Sokolik et al. (2001) point out that the major unknowns concerning dust aerosols are: the size distribution of the particles that span a range from 0.01 to about 100 μm, the vertical and spatial variability within the dust plumes and optical properties like complex refractive index, absorption coefficient, single-scattering albedo, particle shape or the scattering phase function. The single-scattering albedo is the most important factor for the short-wave radiative forcing of mineral dust, whereas the long-wave forcing of dust is dependent on the vertical distribution of the dust (IPCC, 2007).

In the past few years, several field experiments focusing on desert dust were performed. The Saharan Dust Experiment

*Corresponding author.
e-mail: bernadett.weinzierl@dlr.de
DOI: 10.1111/j.1600-0889.2008.00392.x

(SHADE) was conducted in September 2000, in the Cape Verde area. The main aim of SHADE was to determine parameters relevant for computing the direct radiative effect of dust (Tanré et al., 2003). Haywood et al. (2003a) pointed out that one of the optical particle counters (OPCs) responsible for the measurement of particles in the size range between 1 and 23.5 μm did not work correctly during SHADE. As a result, dust size distributions in the super-micron size range had to be estimated from surface-based sun photometry. Similar problems with the optical particle counter occurred during the Southern African Regional Science Initiative (SAFARI) 2000 (Haywood et al., 2003b). The Puerto Rico Dust Experiment (PRIDE) took place in the Caribbean in June/July 2001. Data from a light aircraft, remote-sensing and ground-based measurements were used to study the dust after the transport across the Atlantic into the Caribbean region (Maring et al., 2003; Reid et al., 2003b). Reid et al. (2003a) used the data gathered during PRIDE and compared size and morphological measurements of coarse mode dust particles. They found large differences between OPCs and aerodynamic methods. The results of SHADE, SAFARI and PRIDE suggest that there is still a need for the exact quantification of the dust size distribution up to sizes of 100 μm.

Both experiments, SHADE 2000 and PRIDE 2001, took place in the outflow area of dust on Cape Verde, several hundreds of kilometres away from the major dust sources, so, the dust properties may have been transformed during transport. In contrast, the Saharan Mineral Dust Experiment (SAMUM) was conducted in southern Morocco, close to the Saharan desert, in May/June 2006 (Heintzenberg, 2008). SAMUM focused on the microphysical, optical and radiative properties of pure dust aerosol in a vertical column over the Sahara and during transport to Western Europe. During SAMUM, the microphysical, chemical and optical properties of dust were extensively probed close to the Sahara over Ouarzazate (OZT) and Zagora (ZGA), over Casablanca (CASA) and over Portugal. Important objectives addressed in this study are the vertical structure of the dust layers, which can not be detected by satellite remote sensing or sun photometry, the complete dust particle size distribution, the aerosol mixing state and potential effects of large dust particles with diameters $D_p > 50$ μm. These issues are discussed on the basis of the observations from the Falcon aircraft.

2. Methods

2.1. SAMUM Falcon flights—an overview

During the SAMUM field phase, the DLR Falcon operated from the International Airport Mohammed V in Casablanca (CASA; 33°22′N, 7°35.5′W, 200 m a.s.l.) and took measurements between 18 May and 7 June 2006. The aircraft was mainly cruising between the two ground stations Ouarzazate (OZT; 30°56.5′N, 6°54.4′W, 1150 m a.s.l.) and Zagora (ZGA; 30°21′N, 5°52′W, 820 m a.s.l.) airport (Fig. 1). The flight tracks for all flights performed during SAMUM are summarized in Fig. 1. Details on the flights are compiled in Table 1.

Three large-scale dust events extending from southern Morocco to Portugal occurred during the intensive observation period of SAMUM. The dust events were probed extensively, including horizontal and vertical dust plume structures. The dust events ranging from 16 to 22 May, 24 to 28 May and 31 May to 5 June 2006 are referred to as Episode 1, 2 and 3, respectively. The dust mobilization was different within the three Episodes. In Episode 2 and 3, the dust was frequently mobilized by density currents in the Atlas region, which caused strong turbulent winds along their leading edges (Knippertz et al., 2007). According to Knippertz et al. (2007), dust mobilization by density currents

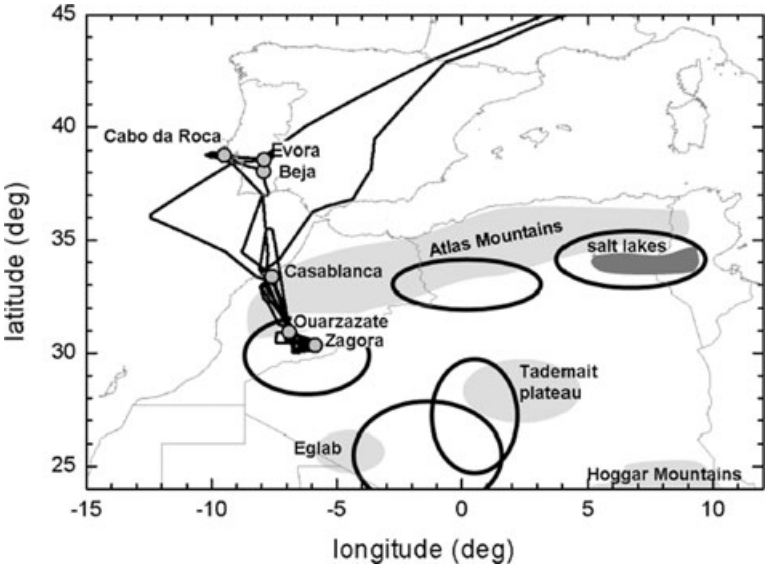

Fig. 1. Map of Northern Africa and Western Europe, with the location of the SAMUM ground sites Ouarzazate and Zagora, the Falcon operation base at Casablanca and the measurement sites at Portugal indicated. The black lines show the flight tracks for all flights performed during SAMUM. The dust source regions (see Petzold et al., 2008) are marked by black circles.

Table 1. Research flights conducted during SAMUM. OP, Oberpfaffenhofen; CASA, Casablanca; OZT, Ouarzazate; ZGA, Zagora. On 19 May, 28 May, and 4 June 2006 the flights were coordinated with the overpasses of the TERRA and ENVISAT satellites with the MISR and MERIS instruments on board.

Mission ID	Date (2006)	Time (UT)	Route	Flight mission
060518a	18 May	07:01–10:15	OP → Beja (Portugal)	transfer flight
060518b		11:33–13:50	Beja → Beja	long-range transport to Europe
060518c		14:44–15:04	Beja → Faro (Portugal)	long-range transport to Europe
060518d		15:55–16:50	Faro → CASA (Morocco)	long-range transport to Europe
060519a	19 May	10:35–12:10	CASA → OZT	closure OZT, MERIS (10:50), MISR (11:11)
060519b		14:35–15:10	OZT → CASA	dust
060520a	20 May	10:34–13:50	CASA → OZT → ZGA → CASA	convective dust layer, closure OZT & ZGA
060522a	22 May	15:04–16:09	CASA → OZT	dust
060522b		17:18–18:15	OZT → ZGA → OZT	low-level dust
060522c		21:23–22:01	OZT → CASA	dust
060527a	27 May	09:15–12:36	CASA → Beja → Evora → CASA	long-range transport to Portugal
060528a	28 May	10:13–13:35	CASA → ZGA→ OZT → CASA	closure ZGA & OZT, MISR (11:05), MERIS (11:08)
060603a	3 June	01:36–04:49	CASA → ZGA→ OZT → CASA	night flight
060603b		07:06–09:09	CASA → ZGA → OZT	early morning flight, closure ZGA & OZT,
060603c		11:04–11:42	OZT → CASA	dust, MERIS (11:19)
060604a	4 June	09:18–12:34	CASA → OZT→ ZGA → CASA	closure OZT & ZGA, MERIS (10:48), MISR (11:11)
060607a	7 June	10:08–10:38	CASA → Spain → OP	long-range transport to Europe

was identified on 7, 13, 25, 31 May and between 2 and 5 June 2006. Details on the dust source regions within the three dust episodes are given in Petzold et al. (2008) and Knippertz et al. (2008). At the time of every dust episode, several research flights close to the source and to Portugal were conducted. During the flight missions, the high spectral resolution lidar (HSRL) acted as a path finder for the in situ measurements (see also Section 2.3). The average aerosol optical depth (AOD) measured by the HSRL south of the Atlas ranged between 0.4 and 0.6.

During Episode 1, dust plumes were extending from Morocco to Portugal. Within this episode, the dust was probed several times (flights #060518b–#060522c) over Cabo da Roca (38°47′N, 9°30′W), Evora (38°31.4′N, 7°54′W) in Portugal, close to the Moroccan coast and over Casablanca. Over Portugal on 18 May, only the northern edge of a thin (about 800 m vertical extent) dust plume was found at altitudes between 3.6 and 4.4 km a.s.l. On 19 May, a well-mixed dust layer was probed over Ouarzazate. In contrast to the 19 May, when almost no clouds were present, the dust layer on 20 May was partially topped by convective cumulus clouds. In Episode 1, the AOD ranged between 0.2 and 0.5 at Ouarzazate airport (Toledano et al., 2008). The highest value of the AOD in Episode 1 occurred on 20 May and decreased towards the end of the episode on 22 May. The flights on 22 May (#060522a–c) were designed to probe the aerosol very close to the surface in the Dra valley near to Zagora. The lowest flight altitude was at 500 m above ground.

Between 24 and 28 May, the second dust event (Episode 2) took place. The dust plumes extended from Morocco to Portugal. During this episode, dust layers were probed several times successfully in the far field over Portugal (#070527a), close to the Atlantic coast of Morocco (#070527a, #070528a) and near the source regions (#070628a).

The last dust event (Episode 3) within the intensive observation period of SAMUM started in the evening of 31 May and reached its maximum strength on 3/4 June. Within Episode 3, four research flights were conducted, including a night flight (#060603a) and an early morning flight (#060603b). During the night flight, the edge of a Saharan dust layer leaving the African continent was nicely detected. Furthermore, the dust layer close to the source was probed before sunrise, before convection became active. The dust layer of flight #060604a showed a clear horizontal and vertical gradient. During the return flight (#060607a) from Morocco to Oberpfaffenhofen on 7 June, a dust plume extended from Morocco to the Pyrenees. The Falcon sampled the dust in situ on constant-altitude sequences over the Atlantic Ocean, thereafter the remaining distance was performed at 11 km, delivering a lidar cross-section from Spain to Oberpfaffenhofen.

The three dust events within the SAMUM observation period gave the opportunity for numerous measurements in dust layers. In total, 4 aged dust layers and 49 pure dust layers were investigated, 37 of which were south of the Atlas Mountains. Altogether, 73 particle size distributions of different aerosol types, including pure dust, aged dust, mixed plumes containing local pollution and dust aerosol, marine aerosol and local pollution aerosol were analysed. On 19 May, 28 May and 4 June 2006, the dust was probed during the overpasses of the TERRA and ENVISAT satellites with the MISR and MERIS instruments,

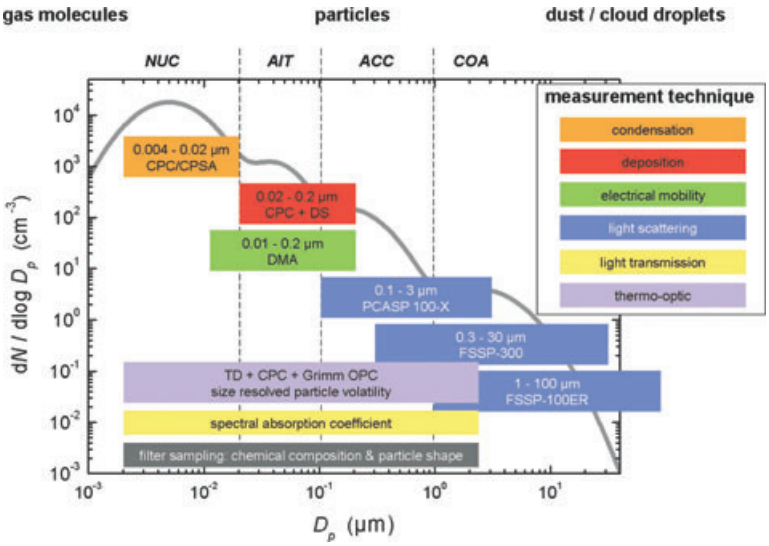

Fig. 2. Schematic of size ranges covered by the in situ measurement techniques of the DLR Falcon instrumentation. NUC, nucleation mode; AIT, Aitken mode; ACC, accumulation mode; COA, coarse mode; CPC, Condensation Particle Counter; CPSA, Condensation Particle Size Analyser; DS, Diffusion Screen Separator; DMA, Differential Mobility Analyser; PCASP-100X, Passive Cavity Aerosol Spectrometer Probe; FSSP, Forward Scattering Spectrometer Probe; TD, thermal denuder AND Grimm OPC, Grimm Optical Particle Counter.

Table 2. Instrumentation on board the Falcon aircraft during SAMUM 2006. The first column displays the name of the instrument, the second column the measured property.

Instrumentation	Property
Aerosol in situ instruments	
CPC/CPSA	size distribution of ultrafine particles ($0.004 < D_p < 0.08$ μm)
DMA	size distribution Aitken mode ($0.01 < D_p < 0.2$ μm)
TD (250°C) + (DS) + CPC	non-volatile fraction in three size ranges (*NUC*, *AIT*, *ACC*)
TD (250°C) + OPC	non-volatile size distribution
PCASP-100X-100X	dry state accumulation mode (0.1 μm $< D_p < 3.0$ μm)
FSSP-300	ambient state accumulation + coarse mode ($0.3 < D_p < 30$ μm)
FSSP-100	ambient state accumulation + coarse mode ($1 < D_p < 100$ μm)
3-λ PSAP	absorption coefficient at $\lambda = 467$, $\lambda = 530$ and $\lambda = 660$ nm
Filter sampling	chemical composition and shape of sub-2.5 μm particles
Lidar instrument	
High spectral resolution lidar (HSRL)	backscatter at $\lambda = 532$, $\lambda = 925$ and $\lambda = 1064$ nm
	extinction coefficient at $\lambda = 532$ nm
	lidar ratio at $\lambda = 532$ nm
	AOD at $\lambda = 532$ and 1064 nm
	depolarization at $\lambda = 532$ and $\lambda = 1064$ nm
	water vapour at $\lambda = 925$ nm
Meteorological data	
Falcon standard instrumentation	*T*, *p*, *RH*, 3-D-wind velocity

respectively. The validation of satellite products with the airborne in situ data is subject of ongoing work.

2.2. SAMUM instrumentation

The SAMUM payload on board the Falcon combined a nadir-looking HSRL (Esselborn et al., 2007), with extensive aerosol microphysics and chemistry in situ instruments. As shown in Fig. 2, the in situ aerosol instrumentation covered the whole particle diameter (D_p) spectrum from the smallest nucleation mode particles to dust particles in the far super-micron range ($0.004 < D_p < 100$ μm). The Falcon standard instrumentation provided data for atmospheric parameters like temperature, pressure, relative humidity and 3-D wind velocity. Table 2 summarizes the instrumentation operated on board of the Falcon aircraft.

The sub-100 nm particle fraction was sized by a set of condensation particle counters (CPCs), which were operated at different cut-off diameters. The different cut-off diameters were partly accomplished by a modification of the instruments supersaturation ratio (Schröder and Ström, 1997; Fiebig et al.,

2005) and partly by a combination of the CPCs with diffusion screen separators (DS). These diffusion screens shift the minimum threshold diameter to 80 and 200 nm, respectively, at free tropospheric conditions of approximately 300 hPa (Feldpausch et al., 2006). The super-100 nm particle fraction was sized by a combination of OPCs of type Grimm 1.109, PCASP-100X, FSSP-300 and FSSP-100. The PCASP-100X, FSSP-300 and FSSP-100 are equipped with de-icing, which is switched on if the outside air temperature drops below 273 K. During SAMUM, this temperature was reached at altitudes between 4–5 km a.s.l. A Differential Mobility Analyser (DMA) was operated in a stepping mode at diameters 0.015, 0.03, 0.05, 0.08, 0.12 and 0.16 μm to check the validity of the CPC + PCASP-100X size distributions.

Apart from the wing-mounted PCASP-100X, FSSP-300 and FSSP-100, all instruments were operated inside the cabin of the Falcon, sampling from an isokinetic inlet. The diameter $D_{50\%,\mathrm{iso}}$, at which 50% of the particles pass the isokinetic inlet, was calculated by Fiebig (2001). At the ground level $D_{50\%,\mathrm{iso}}$ is approximately 2.5 μm and decreases to about 1.5 μm at an altitude of 10 km.

Beyond particle sizing, the instrumentation was designed to provide information on the aerosol absorption coefficient at the wavelengths of 467, 530 and 660 nm with a 3-λ particle soot absorption photometer (PSAP) (Virkkula et al., 2005). The 3-λ PSAP data were used to determine the complex refractive index of desert dust, urban pollution aerosol and marine aerosol particles (more details on this are given in Petzold et al., 2008).

Furthermore, the size distribution of non-volatile aerosol compounds was recorded. For this purpose, three of the CPCs and the Grimm OPC were connected to a thermal denuder (TD) heating the aerosol to 250 °C. Heating the aerosol removes volatile material from the mixed particles (Clarke, 1991). The difference between the size distributions of the total and of the non-volatile aerosol allows the investigation of the aerosol mixing state (see Section 2.5) and complements the chemical analyses of filter samples (Kandler et al., 2008) collected during the flights.

2.3. *Concept for airborne dust measurements during SAMUM*

The design of the SAMUM Falcon flight missions, including descents and ascents through the aerosol layers, was supported by a combined approach of model forecasts studied before the flight and monitoring of characteristic tracers during the flight. The general weather forecast during the SAMUM field experiments was based on forecasts from the European Centre for Medium-Range Weather Forecasts (ECMWF). Furthermore, dust plume forecasts with the DREAM model (Nickovic et al., 2001) were made. During the flights, the HSRL allowed the online monitoring and measurement of the atmospheric stratification, especially the structure of the dust layers. Thus, the HSRL acted as a path finder to direct the aircraft into the plumes to take in situ measurements.

To get good statistics and a large number of data points in a particular plume, constant-altitude sequences (of 5–10-min duration) were flown, resulting in the characteristic stepped flight profile. Fig. 3 sketches a flight profile characteristic for SAMUM. The dotted line shows the flight altitude, the solid line represents the time-series of the dust mode particle concentration and the greyish areas denote the averaging periods for the analysis of dust properties. In most cases, the dust properties were quite homogeneous at a constant altitude so that averaging over one constant-altitude sequence was possible. In case that dust properties changed on a constant-altitude sequence, this level was divided into sub-sequences for the data analysis. For lack of space, only a limited number of sampling devices were mounted in the aircraft. Therefore, chemical samples of particles could be gathered only three times during each Falcon flight. The sampling of particles was mainly conducted on constant-altitude sequences.

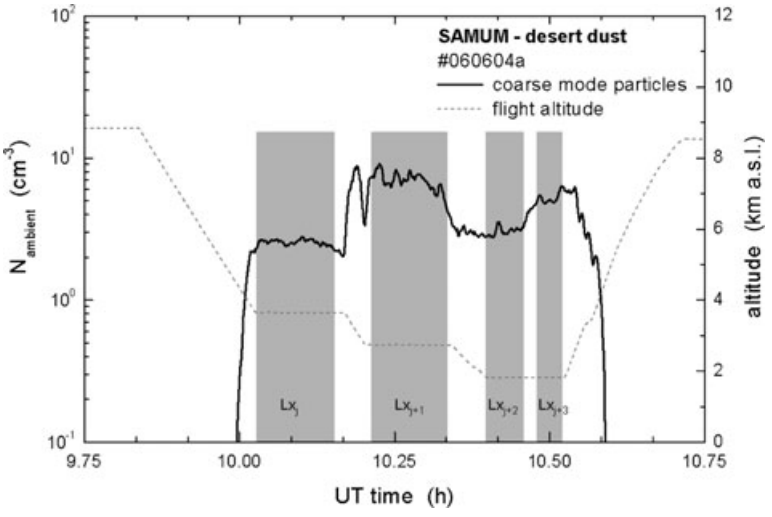

Fig. 3. Time-series of coarse mode particles for the SAMUM research flight on 4 June 2006. The flight altitude is marked by the grey line, and the grey shaded areas indicate the averaging periods. For every Falcon flight, the averaging periods were consecutively numbered with a Layer ID Lx$_j$ (e.g. L03).

2.4. Data analysis

2.4.1. Volumetric units and aerosol modes. The use of volumetric units throughout this work requires explanation. If number or mass concentrations, aerosol absorption coefficients and particle size distribution refer to standard temperature and pressure conditions STP (273.15 K, 1013.25 hPa), they are given as particles per standard cm^{-3} (scm^{-3}). The STP concentration data correspond to mixing ratios, which are independent of ambient pressure and temperature during the measurement. If the concentration data are not explicitly given in STP, they refer to ambient conditions. In the presented tables, the factor f_{STP} necessary for the conversion from STP to ambient conditions is given. Optical properties are calculated from ambient microphysical properties.

2.4.2. Microphysical aerosol properties and data reduction. For this study, the data analysis was reduced to relevant desert dust encounters. The data were averaged over homogeneous constant-altitude sequences and size distributions were calculated. The size distributions were derived from the combined analysis of CPC and PCASP-100X,[1] TD, CPC and Grimm OPC[2] and FSSP-300 data with a newly developed inversion algorithm (Fiebig et al., 2005). Here, only size distributions measurements out of cloud are presented.

Since the inversion of the OPC data requires an assumption on the refractive index, the size distributions in desert dust, urban and mixed plume probes were inverted using the refractive indices derived from the 3-λ PSAP measurements (Petzold et al., 2008) for the respective averaging period. For the tropopause region outside of dust plumes, a refractive index of $m = 1.40 + 0.0i$ was used, whereas for the clean troposphere a refractive index of $m = 1.53 + 0.0i$ was assumed to be appropriate.

Desert dust size distributions were derived from PCASP-100X and FSSP-300 data under the assumption of spherical shape, although dust particles are of non-spherical shape. A very recent study on the measurement of mineral aerosol size distributions with laser particle sizing instruments (recording the scattered light at various angels close to the forward direction) concluded that size distributions derived from optical probes using Mie theory are a useful estimate for the true desert dust size distribution (Veihelmann et al., 2006). *PM2.5* time-series were inferred from the aerosol volume by assuming a particle density of 2600 kg m^{-3} (Hess et al., 1998) for desert dust encounters.

2.4.3. Assessment of size distribution uncertainties. Several publications deal with the interpretation of the data from optical spectrometers and possible error sources. For example Borrmann et al. (2000) show the impact of non-spherical particles on the FSSP-300, and Strapp et al. (1992) look at the differences in PCASP-100X and FSSP-300 due to hydration. An error analysis of the FSSP-300 is presented in Baumgardner et al. (1992). In general, several factors are contributing to the measurement accuracy of optical spectrometer probes, including uncertainties in the sampling volume, inadequate sampling statistics, uncertainties in the refractive index, or particle asphericity. However, significant improvements in the measurement uncertainties can be made if information is available about the chemical composition of the particles (Baumgardner et al., 1992). To asses the errors introduced in the data analysis by uncertainties in the refractive index, the sensitivity of the inverted size distribution from the CPC + PCASP-100X and the FSSP-300 was tested for several refractive indices, which covered the spectrum of refractive indices observed during SAMUM. Results of the sensitivity study are shown in Fig. 4. The top panel shows the number size distribution between $0.01 < D_p < 30$ μm, whereas the bottom panel shows the surface distribution for the same case in the diameter range $0.1 < D_p < 30$ μm. Note that the *y*-axis in the bottom panel is plotted on a linear scale to visualize the differences for different refractive indices. The size distribution of non-absorbing particles appears to be rather insensitive to the variation of the real part of the refractive index for both instruments (not shown). The size distribution of the CPC + PCASP-100X is even insensitive to the variation of the imaginary part of the refractive index for particles $D_p < 0.6$ μm (Fig. 4, circles), whereas for larger particles with increasing imaginary part the size distribution slightly changes. In contrast, the size distribution derived from the FSSP-300 (Fig. 4, triangles) is more sensitive to the variation of the imaginary part of the refractive index: an increasing absorption shifts the size distribution towards larger particle sizes. During SAMUM, the FSSP-300 was very important due to the large sizes of the dust particles. In Fig. 4, the data from #060519a, L02 were inverted with different refractive indices. The refractive indices used cover the spectrum of refractive indices derived for all SAMUM dust cases with the PSAP-method, including the cases with the largest/lowest imaginary part observed during SAMUM. The particle number concentration of the PCASP-100X and the FSSP-300 is in close agreement (<10% deviation) in the overlap region of both instruments, only with the refractive index derived for #060519a, L02 (red symbols). The assumption of exclusively light scattering particles (Fig. 4, blue symbols) results in a deviation between PCASP-100X and FSSP-300 particle concentration in the overlap region of both instruments of more than 30%. Concluding, the derivation of a reliable dust size distribution from optical instruments requires detailed knowledge of the respective complex refractive index.

The complex refractive indices determined by the 3-λ PSAP and by chemical analyses of the dust samples agree within 30% (Petzold et al., 2008). In a parameter study, we analysed the influence of this refractive index uncertainty on the dust effective diameter D_{eff}, which we used as a measure for the dust size

[1]Henceforth, the notation CPC + PCASP refers to the combined data inversion with the inversion algorithm.

[2]The notation TD + CPC + Grimm OPC also refers to the combined data inversion with the inversion algorithm.

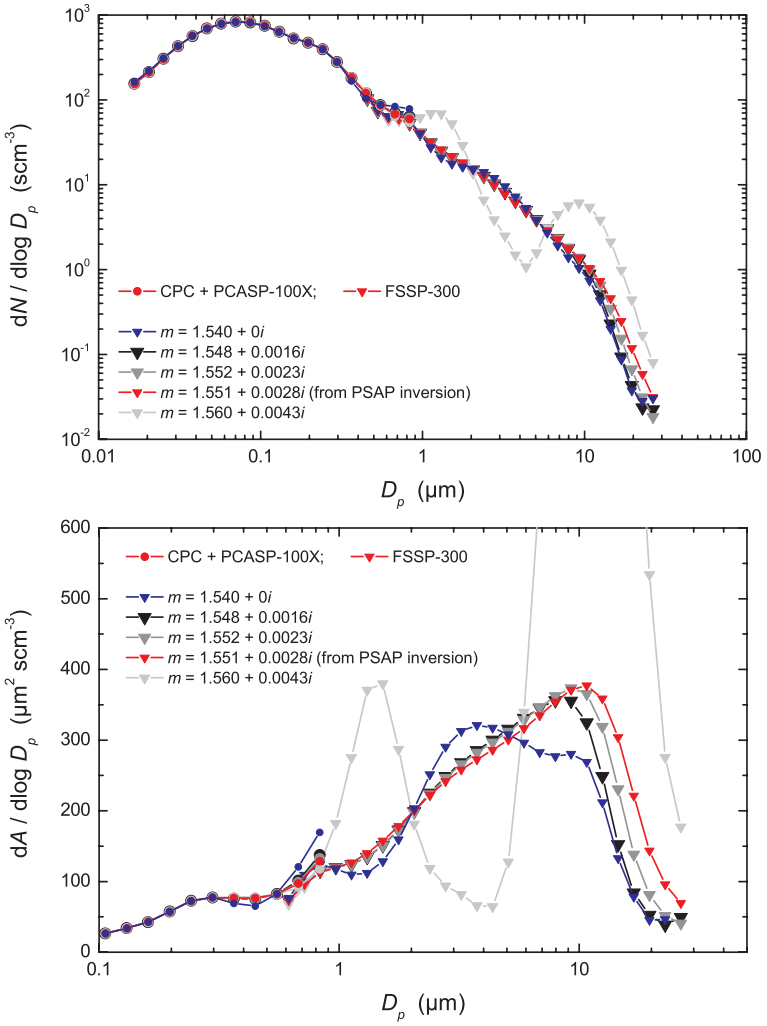

Fig. 4. Sensitivity of particle size distribution derived from the inversion of CPC + PCASP-100X (circles) and the FSSP-300 (triangles) to the chosen refractive index. The top panel shows the number size distribution, whereas the bottom panel shows surface distribution for the same case. Note that the scale is different in the bottom panel and that the *y*-axis is plotted on a linear scale to visualize the differences for different refractive indices. The red curve shows the refractive index derived by the PSAP method. The blue curve shows a case without light absorbing particles, and the grey and black curves show refractive indices derived for other SAMUM cases, including the cases with the largest/lowest imaginary part found with the PSAP method during SAMUM.

distribution. The effective diameter is defined by (Hansen, 1971)

$$D_{\text{eff}} = \frac{\int_0^\infty D_{\text{p}}^3 n\left(D_{\text{p}}\right) \mathrm{d}D_{\text{p}}}{\int_0^\infty D_{\text{p}}^2 n\left(D_{\text{p}}\right) \mathrm{d}D_{\text{p}}}.$$

With the aid of D_{eff}, the influence of the refractive index uncertainty on the derived size distribution is evaluated. To estimate the upper limit of this influence, a dust size distribution that extended to $D_{\text{p}} \sim 40\ \mu$m was taken, and the imaginary part of the refractive index was varied by ±10%, ±20% and ±50%. For all cases, the D_{eff} was calculated. An uncertainty of ±10% (±20%, ±50%) in the imaginary part of the refractive index yielded a change in D_{eff} of 3–4% (3–5%, 5–8%, respectively). These results suggest that the uncertainty introduced in the derived size distributions by uncertainties in the PSAP method can be regarded as minor.

2.4.4. Parametrization of size distributions. To describe particle size distributions in optical models, it is required to formulate a mathematical expression for the measurements with a few adjustable parameters. The most popular expressions are the Junge power law, the log-normal distribution and a modified gamma distribution. In this study, the obtained size distributions are parametrized by fitting multimodal log-normal distributions of the type (Hinds, 1999)

$$\frac{dN}{d\log D_p}\left(ModeX_j\right) = \frac{N_j}{\sqrt{2\pi}\cdot\log GSD_j}\cdot\exp\left[-\frac{1}{2}\left(\frac{\log D_p - \log CMD_j}{\log GSD_j}\right)^2\right]$$

where N_j denotes the particle number concentration in mode X_j, CMD_j is the count median diameter and GSD_j is the geometric standard deviation. GSD_j quantifies the width of the distribution and 68% of the area below the curve is in the range CMD_j $\pm GSD_j$. The so-called mode parameters N_j, CMD_j and GSD_j completely describe one mode of the aerosol size distribution. It turned out that four modes are needed for an adequate representation of the observed dust size distributions.

The quality of the parametrizations was controlled by comparing effective diameter calculated directly from the inverted data

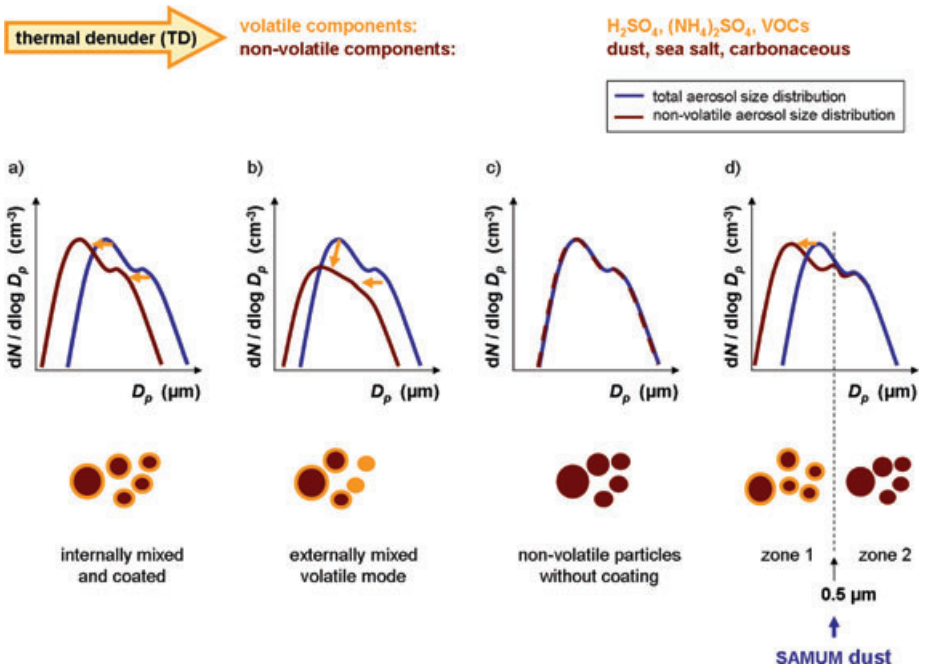

Fig. 5. Schematic illustrating the derivation of the aerosol mixing state on the basis of volatility analyses (see text).

D_{eff} (data) and from the parametrization D_{eff} (mode) using the Hatch–Choate conversion equations (Hatch and Choate, 1929; Hinds, 1999). The parametrizations were regarded as adequate when the deviation between D_{eff} (data) and D_{eff} (mode) was smaller than 7.5%. In 91% of the cases, the deviation between parametrization and data was smaller than 5% and in 60%, it was even smaller than 3%.

2.5. *Aerosol mixing state*

The mixing state of the aerosol was analysed by a combination of particle sizing instruments with a TD (Clarke, 1991). This combination allows the determination of the volatile and non-volatile[3] particle fractions with a high resolution in time and space. The heating temperature of the TD used during SAMUM was set to 250 °C for separating high to medium volatile organics and components of sulphuric acid-like and ammonium sulphated-like behaviour from non-volatile or refractory components like BC, sea salt, dust and crustal material. As mentioned earlier, three CPCs and the Grimm OPC were connected to the TD during SAMUM. With this configuration the derivation of the non-volatile size distribution for particles $D_{\mathrm{p}} < \sim 2.5$ μm was possible.

[3]In this paper, the term 'non-volatile' refers to particles that are non-volatile at a temperature of 250 °C. It is possible that particles that are being called non-volatile in this paper are volatile at higher temperatures.

Figure 5 illustrates how the aerosol mixing state is inferred from these volatility measurements. To investigate possible coatings on the particle, the total (blue lines) and the non-volatile (brown lines) aerosol size distributions are compared. In an internally mixed and coated aerosol (Fig. 5a), the total and the non-volatile size distribution have the same shape, but the maxima of the non-volatile size distribution are shifted to smaller particle sizes. In an externally mixed aerosol that contains a number of totally volatile particles, the shape of the total and the non-volatile size distribution differ (Fig. 5b). In a non-volatile aerosol without coatings, the total and the non-volatile size distribution would be identical (Fig. 5c). As it will be discussed later, the SAMUM dust aerosol evinced two zones of different mixing states, with coated particles below 0.5 μm and non-volatile particles beyond 0.5 μm (Fig. 5d).

3. Results

3.1. *Properties of dust aerosol layers south of the Atlas Mountains*

Dust layers over Ouarzazate and Zagora at the Saharan border were found to extend from the surface to altitudes of about 4–6 km a.s.l. The internal structure of the dust layers varied from well mixed to stratified. In all cases the dust layers exhibited very sharp upper edges. Table 3 summarizes times of vertical in situ profiles at Ouarzazate and Zagora, the altitude of the upper boundary of the dust layers and the dust layer structure.

Table 3. Dust layer structure over Ouarzazate (OZT) and Zagora (ZGA). OZT and ZGA are situated 1150 m and about 820 m above sea level (a.s.l.), respectively. The atmosphere over ZGA was only probed during selected flights. Cases without vertical profiles over ZGA are indicated by "n.d.".

Mission ID	Time of in-situ measurement OZT/UT	Upper boundary. dust layer OZT/m a.s.l.	Dust layer structure OZT	Time of in-situ measurement ZGA/UT	Upper boundary dust layer ZGA	Dust layer structure ZGA
060519a	11:12–12:12	5130	well-mixed	n.d.	n.d.	n.d.
060519b	14:35–14:42	6900	well-mixed	n.d.	n.d.	n.d.
060520a	12:33–13:27	5500–5560	well-mixed	11:29–12:28	5980	well-mixed
060522a	15:30–16:04	6620	well-mixed	n.d.	n.d.	n.d.
060522b	17:18–17:24	low-level	well-mixed	17:25–18:00	low-level	well-mixed
	18:01–18:15	low-level	well-mixed	n.d.	n.d.	n.d.
060522c	17:24–21:33	4650	well-mixed	n.d.	n.d.	n.d.
060528a	12:19–12:55	4500–4700	well-mixed	11:12–12:15	4020–4040	2-layer structure
060603a	03:18–04:09	4420–4470	2–3-layer structure	high level	∼4500	2–3-layer structure
060603b	08:59–09:09	∼4000	2-layer structure	08:02–08:58	4400	2-layer structure
060603c	11:04–11:18	4480	well-mixed	n.d.	n.d.	n.d.
060604a	09:49–10:43	4680–4840	3-layer structure	11:24–12:04	4720–4820	2-layer structure

It is obvious that stratified layers were observed in the early and late morning, whereas during afternoon and evening flights, well-mixed dust layers were present.

Figure 6 shows two cases, the well-mixed dust layer at Ouarzazate on 19 May and the stratified dust layer at Ouarzazate on 4 June 2006. In the former case, the boundary layer is well developed with potential temperature θ being almost constant ($\theta = 315.2 \pm 0.5$ K) and wind being variable from the surface up to an altitude of about 5 km (Fig. 6a, mid panel). The particle number concentrations are almost constant from the surface to the top of the dust layer (Fig. 6a, left-hand panel), which can be attributed to turbulence within the boundary layer. The dust layer is topped by a strong inversion: within 235 m, potential temperature increases by about 3 K, and particle number concentrations drop by 1–2 orders of magnitude. This high static stability at the top of the dust layer can facilitate the formation of waves triggered, for example, by thermals or convection within the boundary layer (e.g. Hauf and Clark, 1989) or by the Atlas Mountains. The HSRL cross-section (Fig. 6a, right-hand panel) illustrates the homogenous dust layer. As expected, at the upper boundary of the dust layer a wave-like structure is visible. On most days, wave-like structures were present at the top of the dust layer. On 4 June, a three-layer structure over Ouarzazate and a two-layer structure over Zagora is visible in the lidar signal (Fig. 6b, right-hand panel). The different layers over Ouarzazate coincide with different potential temperature gradients and wind signals (Fig. 6b, mid panel). Although the well-mixed boundary layer ($\theta = 308.8 \pm 0.2$ K) reaches up to about 3 km a.s.l. the layer above is characterized by a stable stratification. Between 3 and 4 km a.s.l. advection of dust is taking place, and the upper part of the dust layer is probably the residuum of the lofted boundary layer from the day before. The advection of dust in an altitude of about 3 km was also documented by the IfT-lidar at Ouarzazate (Tesche et al., 2008).

Well-mixed dust layers without major vertical gradients in the concentration of large particles were characteristic for SAMUM. Figure 7 shows averaged vertical profiles of aerosol number concentrations measured during SAMUM. Note the sharp upper boundary of the dust layers. In contrast to the expected vertical gradient in the number concentration of large particles, no significant enhancement of large particles close to the surface and no depletion of large particles close to the top of the dust layer were observed. This is the result of turbulent mixing within the boundary layer. Above the main dust layer, dust filaments were observed on most days and wave-like structures were present at the top of the dust layer.

Figure 8 shows two examples of dust number size distributions (top panels), one measured over OZT at 4853 m a.s.l. on 19 May (L02, left-hand panels) close to the top of the dust layer and one measured over ZGA at 3703 m a.s.l. on 4 June 2006 (L07, right-hand panels). The corresponding surface distributions are shown in the bottom panels of Fig. 8. The measurements correspond to the vertical profiles in Fig. 6. The black symbols depict the non-volatile size distribution, whereas the grey symbols show the total aerosol size distribution. The error bars indicate the standard deviation of the atmospheric particle concentration within the averaging interval. The parametrization of the size distribution is marked by the dashed line. The size distributions of both dust layers exhibit similar microphysical properties. Comparing the non-volatile (black symbols) and the total aerosol size distribution (grey symbols), two ranges with different mixing states and therefore different particle morphology are striking: in the

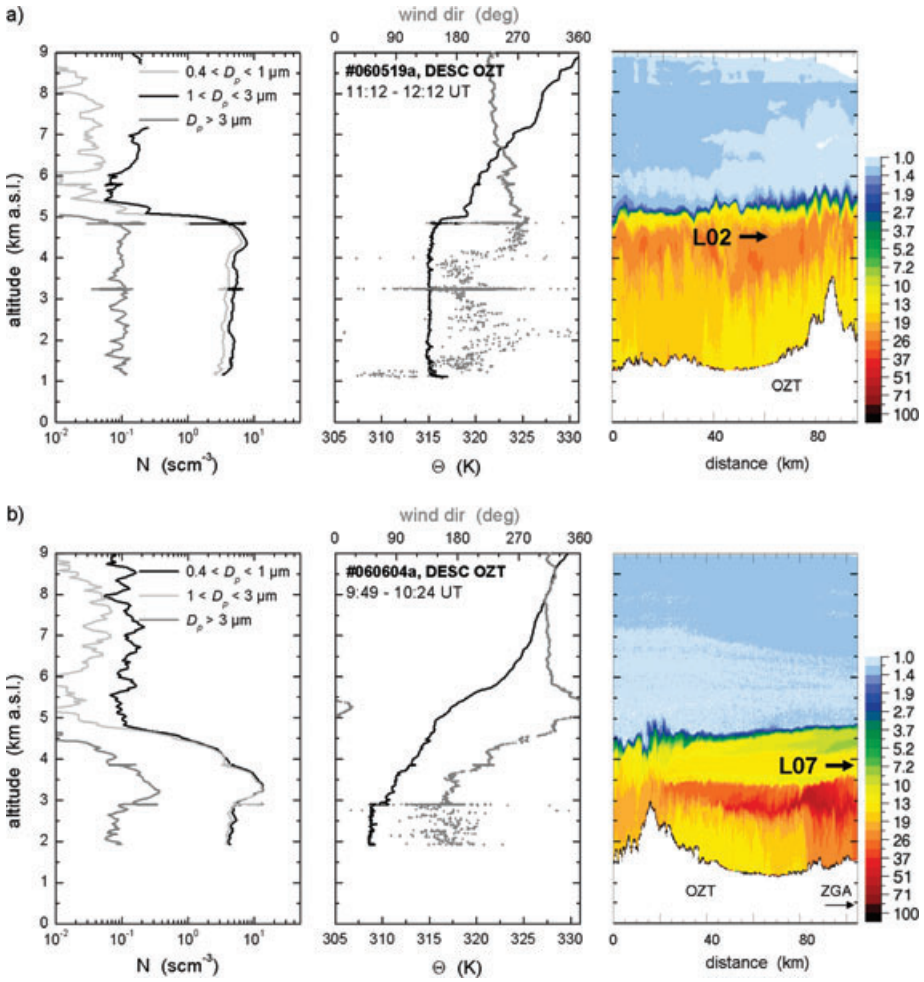

Fig. 6. Vertical structure of (a) the well-mixed dust layer on 19 May 2006 and (b) the 2–3-layer-structure dust layer on 4 June 2006. Both profiles were measured at Ouarzazate. The left-hand panels show profiles of particle number concentration for STP conditions in the size range of $0.4 < D_p < 1$ μm (black line), $1 < D_p < 3$ μm (light grey line) and $D_p > 3$ μm (grey line). The mid panels show potential temperature (black line) and wind direction (grey symbols). In the right-hand panels the dust layer structure is illustrated by HSRL backscatter ratio at 1064 nm (colour coded). The black arrows mark where the size distributions L02 and L07 shown in Fig. 8 were measured.

size range beyond 0.5 μm, the non-volatile and the total size distribution are coinciding, whereas for particles smaller than 0.5 μm, this is not the case. Though the non-volatile size distribution has the same shape and similar particle number concentrations (within 10% deviation) as the total size distribution, the peak of the size distribution is shifted towards smaller particle diameters. This feature suggests that particles smaller 0.5 μm have a non-volatile core with a volatile coating (see also Fig. 5d). According to the results of the volatility analyses, the dust size distribution can be separated into two zones. Zone 1 (below 0.5 μm) is composed of internally mixed and coated particles and zone 2 (above 0.5 μm) is composed of internally mixed particles without coating, which contain light absorbing constituents. The findings of two zones of different mixing states are consistent with hydroscopicity measurements (Kaaden et al., 2008) and chemical analyses of filter samples (Kandler et al., 2008). The excellent agreement between the PCASP-100X and the FSSP-300 suggest that the low humidities in the environment precluded the deliquescence of any of the particles. Furthermore, the particles in zone 2 are completely hydrophobic (Kaaden et al., 2008).

The feature of two zones with different mixing states is obvious in all dust size distributions measured during SAMUM. Figure 9 displays a selection of size distributions measured during different SAMUM flights, including examples for a clean tropospheric size distribution (#060519a, L00), a mixture of dust and urban pollution (#060528a, L14) and urban pollution and marine aerosol (#060527a, L13). The urban pollution aerosol (e.g. #060527a, L13) and the free tropospheric aerosol (#060519a, L00) differ clearly from the dust aerosol. The

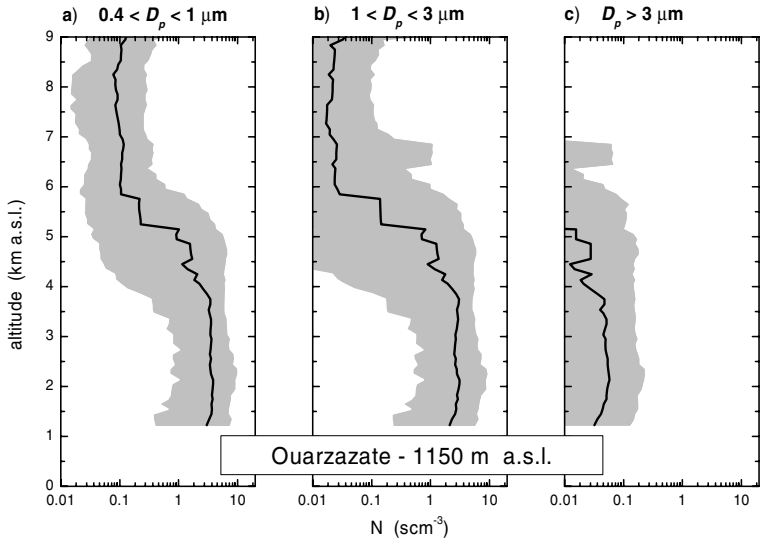

Fig. 7. Average vertical profiles of aerosol number concentration for STP conditions measured during SAMUM: median number concentrations (black line) of particles with diameters D_p (a) $0.4 < D_p < 1$ μm, (b) $1 < D_p < 3$ μm and (c) $D_p > 3$ μm. The grey shaded area represents the range within 10- and 90-percentile values.

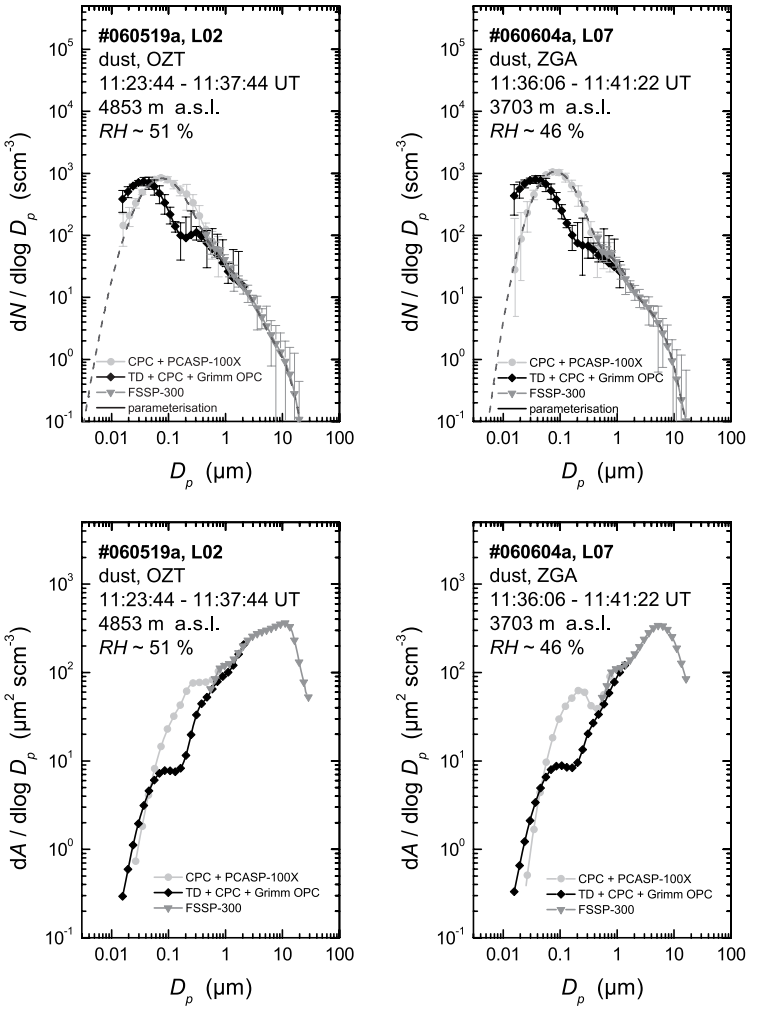

Fig. 8. Composite size distribution of desert dust from CPC, PCASP-100X, Grimm OPC an FSSP 300 for L02 on 19 May over Ouarzazate (left-hand panels) and L07 on 4 June 2006 (right-hand panels). The top panels show particle number distributions, whereas the bottom panels illustrate the corresponding surface distributions. The black line shows the non-volatile size distribution from the combined analysis of the Grimm instrument and heated CPCs, the light grey line shows the size distribution derived from the combined analysis of CPC and PCASP-100X data and the grey line shows data from the FSSP-300. The parametrization is indicated by the dashed line. Particle number and area concentrations refer to STP conditions.

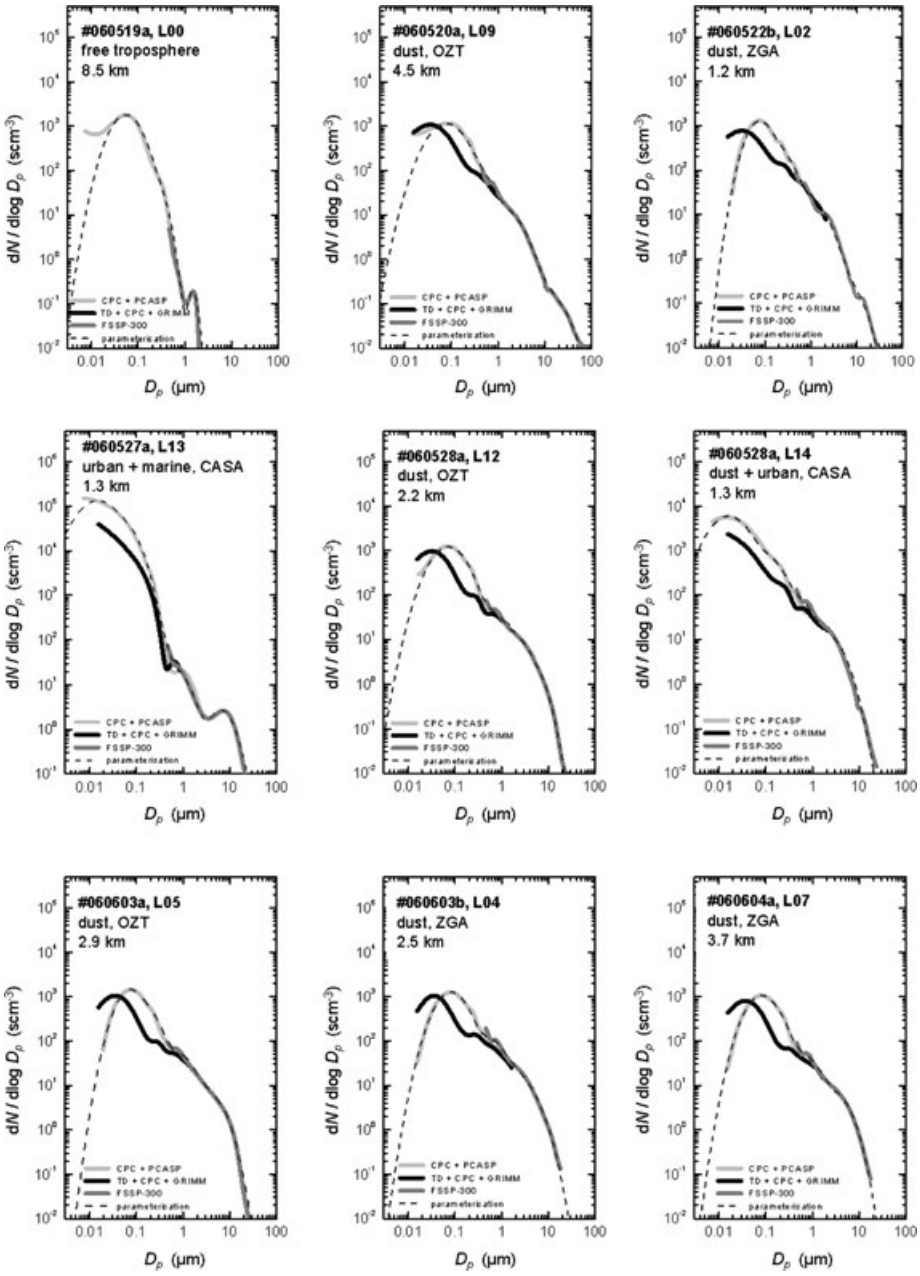

Fig. 9. Examples of size distributions measured during different SAMUM flights, including dust aerosol and examples for a clean tropospheric size distribution (#060519a, L00), a mixture of dust and urban pollution (#060528a, L14) and a mixture of urban pollution and marine aerosol (#060527a, L13). For clarity, no error bars are shown. The dust aerosol shows a characteristic structure with two zones of different mixing states (see text). In the pollution case (#060527a, L13), the number concentration of small particles ($D_\mathrm{p} < 0.1$ μm) is increased by two orders of magnitude.

pollution aerosol exhibits a large number of small ($D_\mathrm{p} < 0.1$ μm), totally volatile particles. The number concentration of the sub-0.1 μm particles in the pollution aerosol is even increased by 1–2 orders of magnitudes compared with the dust aerosol. In the free tropospheric aerosol, the concentration of non-volatile particles is below the detection limit of the Grimm OPC, and coarse mode particles are missing.

Figure 10 shows scanning electron microscope images of particles found in zone 1 (left-hand panel) and zone 2 (right-hand panel). The images confirm the particle morphology inferred from the volatility analyses. The left-hand panel shows ammonium sulphate and dust particles around 350 nm, which correspond to zone 1, while the right-hand panel illustrates dust particles up to sizes of 20 μm, which correspond to zone 2. As

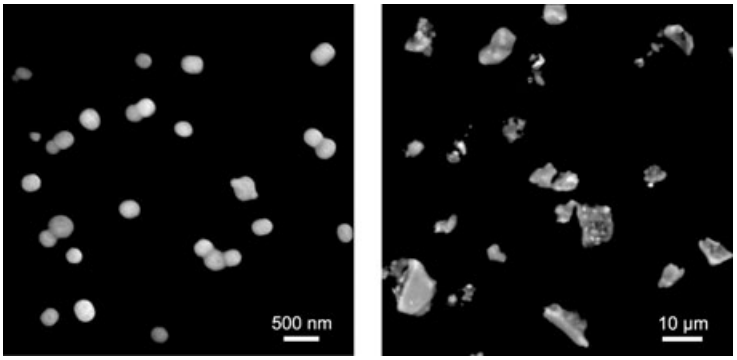

Fig. 10. Secondary electron image of ammonium sulphate and dust particles (left-hand panel) found in desert dust samples around 350 nm and backscatter electron image (right-hand panel) of dust particles up to 20 μm.

a result of the chemical composition, the particles in zone 1 are closer to spherical shape than the particles in zone 2. Table 4 compiles the microphysical properties of the pure dust layers including the flight mission ID and layer ID, start and stop time of averaging sequences, altitude of the measurement and relative humidity during the time of measurement. The parameters of the multimodal log-normal size distribution fits are given for STP conditions. They can be converted to ambient conditions by multiplication of the particle number concentration with f_{STP} (see Section 2.4.1). From the particle number size distribution, every other distribution such as volume and surface distribution can be easily be calculated, as all those quantities are proportional to the particle size raised to a power. The *PM2.5* and total mass *(TSP)* concentrations refer to spherical particles of a density of 2600 kg m^{-3} (Hess et al., 1998). On average *PM2.5* contributes only 7 $\pm$ 5% to the total mass; the aerosol mass is dominated by the coarse mode particles. The ratio *PM2.5/TSP* ($f_{PM2.5\,/\,TSP}$) is dependent on the height of the sampled dust layer. Although *PM2.5* contributes about 3–4% to the total mass at 5 km altitude a.s.l., the contribution increases to 10–15% close to the surface, indicating a contribution of local pollution at lower levels. For particles smaller 2.5 μm, the non-volatile volume fraction ($f_{\mathrm{non-vol2.5}}$) ranges around 78 $\pm$ 9%. The geometric standard deviation *GSD* of the dust mode (GSD_{mode4} in Table 4) ranges between 1.42 and 2.33. The count median diameter $CMD_{\mathrm{mode\ 4}}$ of the dust mode varies between 2.3 and 9.5 μm. The associated average effective diameter D_{eff} is 6.5 $\pm$ 2.5 μm.

3.2. Properties of dust layers over Casablanca

Over Casablanca, situated at the Atlantic coast of Morocco, only lofted dust plumes were observed. The atmosphere over Casablanca always exhibited a typical structure with quite a polluted boundary layer at the surface and a lofted dust layer in the altitude range between 1 and 6 km a.s.l. Sometimes the boundary layer and the lofted dust layer were separated by a thin layer of very clean air. The dust layers were characterized by a very sharp lower and upper boundary, within several 200–300 m the particle concentration changed by more than one order of magnitude. On average the lower boundary of the dust layer was located at 1320 $\pm$ 420 m a.s.l. Small lower limits tended to occur during the night flight #060603a and early day flights. The mean upper boundary was found at 4660 $\pm$ 910 m. High upper dust layer boundaries of >5800 m tended to occur in the afternoon. On average, the dust layers had a depth of 3350 $\pm$ 1030 m.

The microphysical properties found in the dust layers over Casablanca were very similar to those found over Ouarzazate and Zagora. Again, the size distribution showed 2 zones with different mixing states. In zone 1 (below 0.5 μm), the particles have a non-volatile core with a volatile coating, whereas in zone 2 (above 0.5 μm) the particles consist of an internal mixture of non-volatile components. Table 5 compiles the microphysical properties of the dust layers over Casablanca. The table is organized in the same way as Table 4. The *PM2.5* and *TSP* mass concentrations refer to spherical particles of a density of 2600 kg m^{-3}. On average *PM2.5* contributes 9% to the total mass. In contrast to the dust layers over Ouarzazate and Zagora, the ratio *PM2.5/TSP* does not show a height dependence. For particles smaller 2.5 μm the non-volatile volume fraction $f_{\mathrm{non-vol2.5}}$ ranges around 70 $\pm$ 9%. This is still within the standard deviation of the mean non-volatile fraction over the source, but with a tendency to increased volatile components. The mean D_{eff} in the dust over Casablanca was 6.0 $\pm$ 2.6 μm, which is close to the values found over Ouarzazate and Zagora.

4. Discussion

4.1. Evaluation of size distributions

4.1.1. Extinction closure. A method to evaluate the particle size distributions is the intercomparison of extinction coefficient calculated from the in situ size distribution measurements with the direct measurements of the extinction coefficient with the HSRL. For that purpose, the microphysical dust properties described in the preceding sections (parametrized size distribution, refractive index and aerosol mixing state) entered an aerosol optical model, which allows the calculation of spectral aerosol optical properties like extinction coefficient or single-scattering albedo. The aerosol optical model is based on the Bohren and Huffman (1983) Mie code for the treatment of spherical particles and

Table 4. Microphysical properties of pure dust aerosol over Ouarzazate (OZT) and Zagora (ZGA)

Mission ID	Layer ID	Site	Start time (UT)	Stop time (UT)	Altitude (m a.s.l.)	RH (%)	f_{STP}	N_{mode1} (scm^{-3})	CMD_{mode1} (μm)	GSD_{mode1}	N_{mode2} (scm^{-3})	CMD_{mode2} (μm)	GSD_{mode2}	N_{mode3} (scm^{-3})	CMD_{mode3} (μm)	GSD_{mode3}	N_{mode4} (scm^{-3})	CMD_{mode4} (μm)	GSD_{mode4}	TSP (data) ($\mu g\ m^{-3}$)	*PM2.5* (data) ($\mu g\ m^{-3}$)	$f_{PM2.5/TSP}$ (%)	$f_{non-vol2.5}$ (%)	D_{eff} (data) (μm)
060519a	L02	OZT	11:23:44	11:37:44	4853	51	0.574	670	0.077	2.10	30	0.44	1.90	11	1.40	1.90	0.70	6.50	1.66	1189	68.9	5.8	83.4	6.5
060519a	L03	OZT	11:44:02	12:06:28	3246	26	0.662	900	0.079	2.30	10	0.55	1.50	8.3	1.40	1.90	0.58	6.50	1.74	1026	52.2	5.1	81.3	6.8
060520a	L02	ZGA	11:38:16	11:48:36	5169	64	0.556	620	0.077	1.90	75	0.24	1.60	32	0.78	1.95	2.00	6.20	1.76	2800	72.5	2.6	80.9	9.9
060520a	L03	ZGA	11:48:36	11:51:01	5170	66	0.556	590	0.074	1.93	80	0.32	1.70	27	1.18	1.94	1.80	6.21	1.95	5065	110.4	2.2	63.3	12.2
060520a	L04	ZGA	11:55:32	12:10:36	3242	27	0.662	800	0.076	1.90	75	0.20	1.55	16	0.66	1.97	1.00	4.75	1.92	1016	31.6	3.1	84.3	8.8
060520a	L05	ZGA	12:10:36	12:18:32	3242	25	0.661	700	0.075	1.90	85	0.20	1.90	14	0.90	2.15	0.50	5.65	1.72	697	47.0	6.7	78.3	5.9
060520a	L07	OZT	12:41:48	12:50:12	5176	75	0.556	900	0.077	2.30	15	0.55	1.50	14	1.25	1.90	1.10	6.50	1.75	1908	74.7	3.9	79.6	8.2
060520a	L08	OZT	12:54:36	13:09:36	3247	26	0.659	1000	0.071	2.40	15	0.55	1.50	10	1.40	1.95	0.40	6.50	1.75	856	58.1	6.8	77.0	5.9
060520a	L09	OZT	13:11:44	13:14:08	4536	56	0.589	950	0.078	2.15	15	0.55	1.50	9	1.40	1.95	0.15	9.50	2.10	2006	54.6	2.7	95.9	13.7
060522a	L04	OZT	15:53:15	15:57:17	3188	22	0.655	700	0.077	1.70	120	0.22	1.60	14	0.80	2.00	1.05	5.90	1.75	1336	38.0	2.8	69.1	8.6
060522a	L05	OZT	15:58:15	16:00:39	2858	19	0.674	750	0.075	1.75	120	0.22	1.60	14	0.80	2.00	0.90	5.90	1.75	1137	32.4	2.8	80.8	8.6
060522a	L06	OZT	16:01:51	16:04:27	2525	16	0.693	720	0.076	1.65	100	0.23	1.60	14	0.80	2.00	1.15	5.90	1.80	1439	33.3	2.3	95.2	9.4
060522b	L01	OZT	17:21:36	17:31:06	2870	20	0.674	700	0.073	1.70	125	0.21	1.67	15	0.82	2.05	0.13	7.15	1.98	650	35.1	5.4	90.9	7.8
060522b	L02	ZGA	17:34:48	17:53:42	1220	9	0.772	700	0.075	1.67	125	0.22	1.67	19	0.82	2.00	0.13	6.55	1.77	369	47.1	12.6	79.9	4.4
060522b	L03	ZGA	17:56:26	18:06:16	2875	20	0.674	700	0.073	1.70	125	0.21	1.67	13	0.82	2.05	0.09	7.15	2.33	881	33.3	9.8	97.4	11.0
060528a	L03	ZGA	11:26:37	11:35:32	3206	26	0.668	950	0.072	1.90	7.5	0.60	1.50	4.7	1.44	2.12	0.26	6.40	1.47	459	27.3	6.0	83.8	5.3
060528a	L04	ZGA	11:41:07	11:46:01	1914	32	0.748	900	0.069	2.05	18	0.55	1.50	14	1.40	1.90	0.30	6.50	1.60	688	72.2	10.5	71.6	4.8
060528a	L05	ZGA	11:46:01	11:48:02	1912	26	0.747	980	0.074	2.05	9.5	0.62	1.45	10	1.30	1.92	0.34	7.95	1.42	625	52.6	8.4	82.0	5.1
060528a	L06	ZGA	11:51:47	11:54:52	1280	22	0.786	950	0.069	2.05	18	0.55	1.50	11	1.40	1.85	0.20	6.50	1.60	470	60.3	12.8	76.8	4.2
060528a	L10	OZT	12:42:42	12:49:47	3870	61	0.630	880	0.077	2.07	11	0.69	1.50	11	1.35	2.05	0.59	6.55	1.65	1153	59.8	5.2	69.4	6.9
060528a	L11	OZT	12:52:02	12:54:02	2907	37	0.684	900	0.077	2.05	9	0.67	1.45	13	1.25	2.10	0.28	6.50	1.75	867	57.0	6.6	72.4	6.1
060528a	L12	OZT	12:55:57	12:59:07	2194	29	0.728	950	0.072	2.05	9	0.67	1.45	13	1.25	2.10	0.24	6.25	1.45	591	56.5	9.6	79.6	4.6
060603a	L04	OZT	03:39:53	03:44:53	3798	81	0.633	880	0.077	1.70	100	0.20	1.50	33	0.65	2.10	2.00	4.40	1.75	1194	62.6	5.2	75.6	6.5
060603a	L05	OZT	03:46:41	03:56:45	2855	49	0.689	880	0.075	1.75	100	0.22	1.50	45	0.65	2.10	2.50	4.40	1.70	1113	77.0	6.9	78.0	5.5
060603b	L03	ZGA	08:16:58	08:27:52	3814	74	0.632	900	0.083	1.80	15	0.55	1.70	7.4	1.40	2.11	0.50	6.50	1.51	819	45.2	5.5	69.2	6.0
060603b	L04	ZGA	08:31:07	08:39:55	2534	39	0.710	890	0.083	1.90	50	0.55	1.69	19.5	1.35	2.10	0.95	4.40	1.68	1267	116.9	9.2	58.1	5.1
060603b	L05	ZGA	08:44:07	08:50:31	1195	28	0.799	1100	0.072	1.80	100	0.40	1.73	22	1.35	1.95	0.30	6.51	1.54	884	126.4	14.3	65.4	4.0
060603b	L06	ZGA	08:55:16	08:58:31	3816	76	0.633	750	0.077	1.85	100	0.20	1.50	18	0.65	2.10	2.50	2.30	1.55	181	47.6	26.2	76.6	2.5
060603b	L07	OZT	09:01:43	09:03:04	2487	44	0.713	800	0.075	1.75	120	0.22	1.50	33	0.60	2.30	1.50	5.00	1.60	899	57.2	6.4	68.2	5.4
060603b	L08	OZT	09:04:16	09:05:04	2356	48	0.723	880	0.073	1.80	100	0.20	1.50	40	0.60	2.10	3.80	3.70	1.85	1498	70.9	4.7	74.0	6.7
060604a	L03	OZT	10:02:18	10:10:02	3854	39	0.629	560	0.075	1.80	75	0.22	1.48	39	0.49	2.38	1.38	4.38	1.69	714	54.5	7.6	82.3	5.2
060604a	L04	OZT	10:12:26	10:20:22	2895	58	0.691	800	0.073	2.00	70	0.20	1.50	75	0.62	2.19	4.50	3.66	1.74	1558	138.9	8.9	82.3	5.1
060604a	L05	OZT	10:24:14	10:31:22	1928	44	0.753	4600	0.010	2.96	330	0.13	1.70	41	0.59	2.09	3.00	3.20	1.74	701	75.4	10.8	99.2	4.4
060604a	L07	ZGA	11:36:06	11:41:22	3703	46	0.639	670	0.077	1.85	90	0.16	1.70	35	0.60	2.06	2.40	3.78	1.68	704	57.9	8.2	70.2	4.8
060604a	L08	ZGA	11:45:38	11:50:02	1938	37	0.752	840	0.072	1.85	90	0.16	1.65	35	0.53	2.30	1.00	4.67	1.58	512	51.1	10.0	73.3	4.3
060604a	L09	ZGA	11:53:10	11:54:50	1288	26	0.793	850	0.072	1.80	90	0.16	1.65	50	0.50	2.10	2.35	3.28	1.74	559	64.4	11.5	78.2	4.2

Note: Size distributions were derived on constant-altitude sequences out of cloud. Besides start and stop time for each averaging interval, the altitude of the measurements, and the relative humidity (RH) are given. N_j, CMD_j, and GSD_j result from log-normal fitting and denote the particle number concentration in mode X_j, the count median diameter, and the geometric standard deviation. All mode parameters are given for STP conditions and can be converted to ambient conditions by multiplication with f_{STP}. The *PM2.5* mass concentration ($D_p < 2.5\ \mu$m) and total mass (TSP) concentration refer to spherical particles of a density of 2600 kg m^{-3}; $f_{PM2.5/TSP}$ is the ratio of *PM2.5* and TSP, and $f_{non-vol2.5}$ is the non-volatile volume fraction in the sub-2.5 μm size range. The effective diameter D_{eff} (data) was calculated from the measurements. The effective diameter can be derived also from the parametrized size distributions via the Hatch-Choate conversion equations (D_{eff} (mode)).

Table 5. Microphysical properties of pure dust layers over Casablanca (CASA). For label see Table 4.

Mission ID	Layer ID	Site	Start time (UT)	Stop time (UT)	Altitude (m a.s.l.)	RH (%)	f_{STP}	N_{mode1} (cm^{-3})	CMD_{mode1} (μm)	GSD_{mode1}	N_{mode2} (cm^{-3})	CMD_{mode2} (μm)	GSD_{mode2}	N_{mode3} (cm^{-3})	CMD_{mode3} (μm)	GSD_{mode3}	N_{mode4} (cm^{-3})	CMD_{mode4} (μm)	GSD_{mode4}	TSP (data) ($\mu g\,m^{-3}$)	*PM2.5* (data) ($\mu g\,m^{-3}$)	$f_{PM2.5/TSP}$ (%)	$f_{non-vol2.5}$ (%)	D_{eff} (data) (μm)
060518d	L02	CASA	16:24:40	16:27:26	4189	51	0.608	500	0.095	2.20	50	0.22	1.50	28	0.90	2.10	1.55	4.90	1.74	1346	81	6.1	64.5	6.5
060518d	L03	CASA	16:29:46	16:35:24	3226	28	0.662	620	0.075	1.95	70	0.22	1.50	28	0.60	2.30	0.83	6.10	1.78	1423	48	3.4	70	8.7
060519b	L02	CASA	14:51:52	14:53:46	4568	46	0.590	500	0.110	1.90	55	0.20	1.55	25	0.72	2.30	1.20	5.80	1.65	1300	60	4.6	66.1	6.8
060519b	L03	CASA	14:54:45	14:57:16	4251	44	0.607	650	0.087	2.20	40	0.20	1.45	32	0.60	2.30	1.85	5.80	1.78	2250	62	3.2	71.5	9.2
060522a	L01	CASA	15:09:27	15:10:23	3819	27	0.627	800	0.073	1.90	6	0.66	1.60	2	1.40	2.15	0.23	8.70	1.50	610	17	2.8	89.6	8.0
060527a	L10	CASA	12:18:14	12:21:09	4169	74	0.676	950	0.073	1.80	30	0.35	1.45	50	0.73	2.47	–	–	–	1104	109	9.9	70	5.0
060527a	L11	CASA	12:23:44	12:26:39	3217	42	0.736	1250	0.073	2.00	30	0.49	1.52	62	1.00	2.37	–	–	–	2536	201	7.9	54.1	5.8
060603a	L09	CASA	04:29:41	04:32:41	3829	81	0.632	1350	0.067	2.15	80	0.20	1.45	15	0.70	2.00	2.30	4.80	1.83	1900	40	2.1	71.4	8.7
060603a	L12	CASA	04:43:41	04:45:41	926	32	0.833	1180	0.073	1.85	90	0.18	1.50	7.6	0.64	2.18	0.31	5.53	1.42	179	18	10	67.9	3.1
060607a	L01	CASA	10:13:30	10:17:54	2588	38	0.705	620	0.084	1.73	45	0.22	1.48	19	0.51	2.29	0.04	6.52	1.42	121	30	25	72.1	2.5
060607a	L02	CASA	10:20:42	10:25:46	3880	36	0.628	700	0.077	1.80	45	0.22	1.48	15	0.51	2.29	0.03	6.45	1.59	94	20	21.9	76.6	2.3

on the Toon and Ackerman (1981) Mie code for the treatment of coated spheres. This aerosol optical model includes a look-up table of common spectral refractive indices available in the literature.

The aerosol optical model is capable of treating internally and externally mixed aerosol modes and coated spheres within the same aerosol. Additionally, the model has a feature that allows the size-dependent specification of the chemical particle composition and the aerosol mixing state. This feature allowed the treatment of the two zones with different mixing states, which were observed in the dust layers. Input data of the aerosol optical model are the integral particle concentration of each log-normal mode ($N_{\mathrm{mode}j}$), the median diameter ($CMD_{\mathrm{mode}j}$), the geometric standard deviation ($GSD_{\mathrm{mode}j}$) and the volume fractions of chemical components within one mode and the mixing state. All parameters can be specified for each mode separately.

Figure 11 depicts two examples of vertical profiles of HSRL extinction measurements (grey lines) and calculated extinction coefficient σ_{ep} (black symbols). In the left- and right-hand panel HSRL extinction measurements at 532 nm and calculated extinction at 532 nm are compared for two cases with stratified dust layers, the 3 June and the 4 June 2006, respectively. Extinction coefficients σ_{ep} calculated from particle size distributions and refractive index data reproduce in all cases the values from direct measurements and reflect the vertical structure of the dust layer, although the calculated σ_{ep} slightly overestimate the values from the direct measurements. Altogether, calculated σ_{ep} (in situ) and measured σ_{ep} (HSRL) were compared for 15 cases. The optical closure between calculated extinction coefficients and HSRL measurements has been achieved successfully as shown in Fig. 12. The data of the lidar–in situ intercomparison are summarized in Table 6. In 53% of the cases, the deviation between HSRL measurements and the in situ calculations is <15%. For extinction coefficients larger 0.05 km^{-1}, the HSRL–in situ difference is between 3% and 26%. Considering the time offset of about 1 h between the HSRL and the in situ measurements, both methods are in good agreement. The deviation between lidar and in situ measurement was larger close to the top of the dust layer than well within the dust layer. One factor causing the larger difference at the top of the dust layer is that the HSRL averages over a particular vertical distance (extinction coefficient: dz ∼250 m), therefore slightly smoothing the sharp upper edge of the dust layer. The largest deviations between HSRL extinction coefficient and calculated extinction coefficient occurred on 27 May 2006, when the dust layer showed a lot of structure and was very inhomogeneous (the 27 May is discussed in Wagner et al., 2008). For this case, good agreement cannot be expected.

The extinction calculated under the assumption of spherical particles was compared with non-spherical calculations conducted at the University of Munich. The effect of non-sphericity on calculated extinction coefficients was smaller than –5% (Wiegner et al., 2008), that is, σ_{ep} was slightly smaller for non-spherical than for spherical calculations. Including

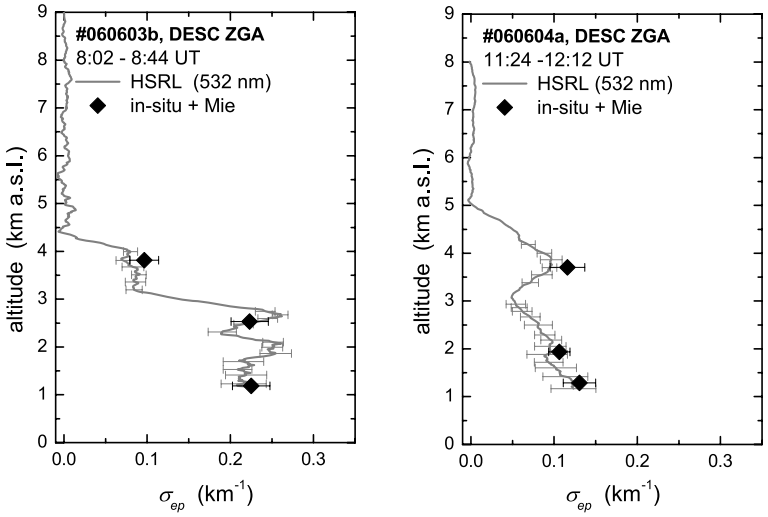

Fig. 11. Vertical profiles of lidar extinction measurements (grey lines) and extinction coefficient calculated from in situ measurements on the basis of Mie theory (black symbols). Both panels show an intercomparison of HSRL extinction measurements at 532 nm and calculated extinction at 532 nm for 3 and 4 June 2006, respectively.

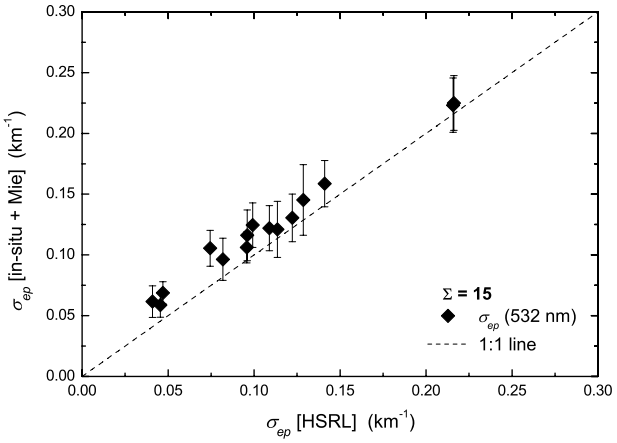

Fig. 12. Closure of extinction coefficient calculated from in situ measurements with Mie theory and measured with the HSRL (532 nm).

particle non-sphericity in the extinction calculation would even improve the agreement between the direct measurements of σ_{ep} with the HSRL and the calculation from the size distribution measurements. These results suggest that the size distribution measurements presented here are representative for the true dust size distribution.

4.1.2. Comparison with other measurements. A comprehensive comparison of the measured size distributions with published information is difficult since different measurement techniques result in different equivalent diameters (e.g. Reid et al., 2003a). In addition, the microphysical dust properties differ for various source regions and distances from the dust source region (Sokolik et al., 1998). Furthermore, most of the existing measurements are ground-based measurements (e.g. Schütz and Jaenicke, 1974; Schütz and Jaenicke, 1978; d'Almeida and Schütz, 1983) whereas the data presented here cover the whole tropospheric column.

Several authors inferred dust properties from satellite measurements or sun photometry, for example, Dubovik et al. (2002) retrieved dust volume distributions from data of the Aerosol Robotic Network (AERONET; http://aeronet.gsfc.nasa.gov/) of ground-based radiometers. The coarse mode volume diameter D_{Vc} for the dust size distributions discussed there can be computed from the parametrized size distributions via the Hatch–Choate conversion equations (Hatch and Choate, 1929; Hinds, 1999) using

$$D_{\mathrm{Vc}} = CMD_{\mathrm{c}} \exp\left(3\,(\ln GSD_{\mathrm{c}})^2\right),$$

where CMD_{c} is the coarse mode median diameter (CMD_{mode4} in Table 4) and GSD_{c} is the geometric standard deviation of the coarse mode (GSD_{mode4} in Table 4).

From the SAMUM size distributions, D_{Vc} was calculated and compared with other existing information. The results of the comparison are shown in Fig. 13. To avoid the influence of deposition during transport, only data which were recorded south of the Atlas Mountains are used in Fig. 13. The age of the dust was between 0–2 d. The very high D_{Vc} occurred preferably in Episode 1. Smaller D_{Vc} occurred when the dust was mobilized by density currents. During flight #060603b, higher and lower D_{eff} were observed. On that day, the dust layer evinced a two-layer structure with different dust origins (Rasp, 2007) and different dust mobilization mechanisms. During flight #060520a on 20 May, very strong convection was going on, which may have mobilized the very large particles. In fact, on that day the largest effective diameters within the whole SAMUM field phase were observed.

A more detailed overview over commonly cited coarse mode particle mass/volume distributions is listed in Table 1 in Reid et al. (2003a). The authors point out that the results derived with optical inversion methods (e.g. AERONET in Fig. 13)

Table 6. Extinction coefficient of dust for lidar/in situ intercomparison levels

Mission ID	Layer ID	Site	Altitude / (km a.s.l.)	σ_{ep} (km^{-1})			
				Lidar	In situ	$\Delta\sigma_{ep}$	Rel. $\Delta\sigma_{ep}$ (%)
060519a	L02	OZT	4853	0.10887	0.12196	0.01309	1.12
060519a	L03	OZT	3246	0.11360	0.12105	0.00745	1.07
060527a	L04	EVO, P	3245	0.04702	0.06883	0.02181	1.46
060527a	L05	EVO, P	2300	0.04548	0.05872	0.01324	1.29
060528a	L03	ZGA	3206	0.04097	0.06157	0.02060	1.50
060528a	L04	ZGA	1914	0.09922	0.12456	0.02534	1.26
060528a	L18	CASA	1729	0.14100	0.15860	0.01760	1.12
060603b	L03	ZGA	3814	0.08192	0.09642	0.01450	1.18
060603b	L04	ZGA	2534	0.21576	0.22324	0.00748	1.03
060603b	L05	ZGA	1195	0.21615	0.22502	0.00887	1.04
060604a	L03	OZT	3854	0.07445	0.10546	0.03101	1.42
060604a	L05	OZT	1928	0.12866	0.14529	0.01663	1.13
060604a	L07	ZGA	3703	0.09598	0.11613	0.02015	1.21
060604a	L08	ZGA	1938	0.09574	0.10624	0.01050	1.11
060604a	L09	ZGA	1288	0.12221	0.13050	0.00829	1.07

Note: The HSRL and the in situ extinction coefficient σ_{ep} are compared at 532 nm. The seventh column shows the difference σ_{ep}(in situ)–σ_{ep}(lidar) and in the eights column the relative deviation σ_{ep}(in situ)/σ_{ep}(lidar) between both methods is presented

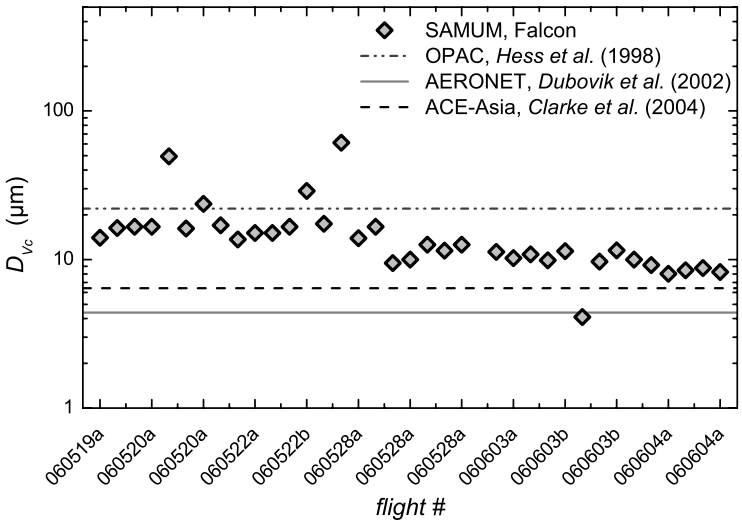

Fig. 13. Intercomparison of coarse mode volume median diameter D_{Vc} derived by different methods. Data are taken from Hess et al. (1998), Dubovik et al. (2002), Clarke et al. (2004) and this study. Except the data from Clarke et al., all measurements refer to African dust.

and with aerodynamic[4] methods group into the same size range (D_{Vc} ~3–7 μm), whereas the results based on optical counter methods are higher ($D_{Vc} > 9$ μm). Reid et al. (2003a) attributed these differences to shortcomings of the OPC. They further reported large differences between the measurements of the FSSP-100 and the PCASP during PRIDE, where the FSSP-100 showed concentrations consistently a factor 2.2 higher than the PCASP. For the SAMUM data, the particle number concentrations measured with the FSSP-300 and the PCASP-100X were in close agreement in the overlap region of both instruments (<5–10% deviation; see also Figs. 8 and 10). The SAMUM data yield an average D_{Vc} of 15.5 $\pm$ 10.9 μm.

Figure 14 (top panel) shows an intercomparison of airborne number size distribution measurements with ground-based methods performed at ZGA during SAMUM. The corresponding surface distributions are depicted in the bottom panel of Fig. 14. The size distributions at the ground were inferred from aerodynamic methods. The ground-based measurements represent the aerosol in the boundary layer below 5 m altitude. Figure 14 indicates close correspondence between the ground-based and the airborne measurements. A more detailed comparison of

[4]Aerodynamic methods size particles based on their mass-to-drag characteristics. The two most common aerodynamic methods are cascade impactors and aerodynamic particle sizers (APS). More detailed information on these instruments can be found, for example, in Hinds (1999).

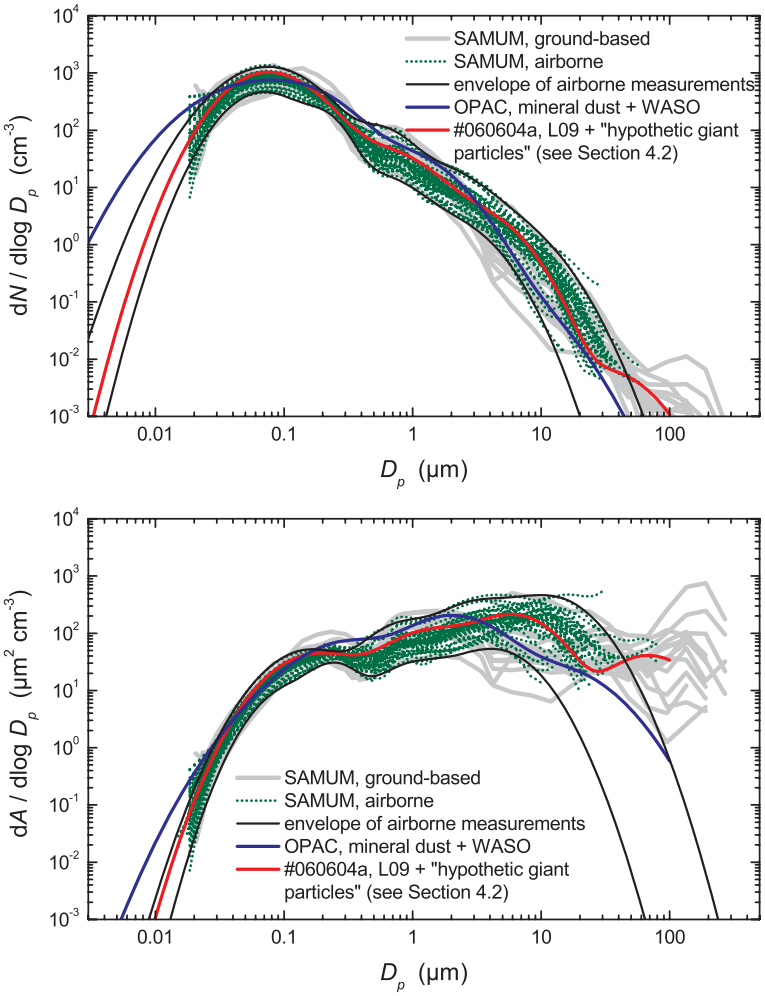

Fig. 14. Intercomparison of SAMUM dust number size (top panel) and surface distributions (bottom panel) measured on board the Falcon (green dotted lines), ground-based measurements (grey lines) performed at Zagora and OPAC values (Hess et al., 1998) for mineral dust (blue line). The red line shows the size distribution L09 recorded during flight #060604a, where a 'hypothetic' saltation mode has been added (see Section 4.2). The black lines are the envelopes of all airborne dust size distributions.

ground-based and airborne measurements for single days revealed good agreement between both methods. In contrast to the airborne measurements, the ground-based measurements show a further mode with a maximum around 100 μm. This is probably the saltation mode, which is only present close to the ground as the large particles settle rather quickly due to gravity.

In addition to the ground-based and airborne measurements, Fig. 14 shows a size distribution modelled with OPAC (Hess et al., 1998). In the OPAC model, a mixture of four components is used to describe desert aerosols: a water soluble component (WASO), and three mineral components of different size—the mineral nucleation mode (MINM), mineral accumulation mode (MIAM) and mineral coarse mode (MICM). The size distribution of the mineral particles depends on the turbidity, that is, the total amount of mineral particles per volume. With increasing total amount of mineral particles, the relative amount of large particles also increases (Koepke et al., 1997; Toledano et al., 2008). This has been taken into account in the data for the aerosol type 'desert' (Hess et al., 1997), which is shown here; however, instead of 2000 particles cm^{-3}, 500 particles cm^{-3} were used for WASO. These data result, under the assumption of 50% relative humidity, in 1 μg m^{-3} for the water soluble component and about 220 μg m^{-3} for mineral dust, in agreement with Kandler et al. (2008), using a cut of diameter of 15 μm.

4.2. *Abundance of giant particles*

The presence of large particles has a significant impact on the radiative effects of dust (e.g. Otto et al., 2007). As it has been shown in Section 4.1, the SAMUM aerosol in situ instrumentation covers the whole range of the dust size distribution. Since the HSRL and the in situ measurements show consistent dust properties, the measured size distribution is representative for the true dust size distribution. Therefore, the abundance of large particles can be investigated in detail. The size of the largest particle measured is determined for all dust sequences over Ouarzazate, Zagora and Casablanca. The maximum particle size measured depends on the detection limit of the FSSP-300; if particle concentrations drop below approximately

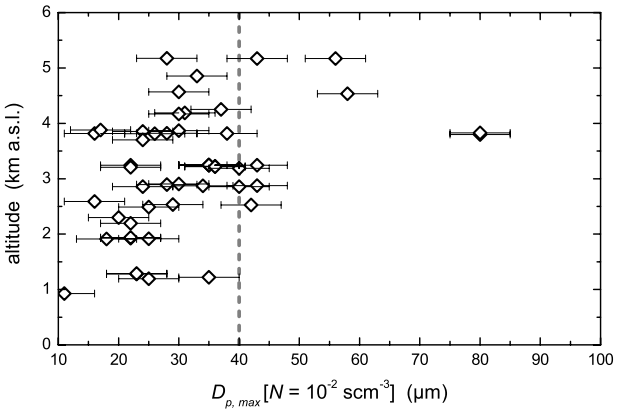

Fig. 15. Vertical distribution of the largest particles detected in each of the pure 49 dust layers investigated (see text). Ouarzazate is located about 1150 m above sea level (a.s.l.). In 80% of the cases the particles were smaller than 40 μm (grey line).

10^{-2} scm^{-3}, the instrument is not able to detect the particles. In our study, we define the maximum particle size, $D_{\mathrm{p,\ max}}$, as the size of the particles that occur at a concentration of 10^{-2} scm^{-3}. Figure 15 shows the vertical distribution of the largest particles detected in each of the pure 49 dust layers investigated. Two findings are obvious from Fig. 15: (1) $D_{\mathrm{p,\,max}}$ shows almost no height dependence and (2) in most cases (80%) the particles were smaller than 40 μm. In all cases, particles larger than 10 μm were present, and in 70% of the measurements, $D_{\mathrm{p,\,max}}$, was between 20–40 μm. The largest particles ($D_{\mathrm{p}} > 50$ μm) at elevated altitudes were observed during flight #060520a, when strong convection was active. To make sure that the in situ measurements had not missed any large particles that were present at concentrations lower than 10^{-2} cm^{-3}, a hypothetic saltation mode has been added to the airborne size distribution measured at L09 on 4 June. The hypothetic saltation mode was chosen such that it was consistent with the measurements at the ground (red line in Fig. 14). Then the extinction coefficient was calculated for the size distribution with and without this hypothetic saltation mode and compared with the direct measurements of the HSRL. Without the hypothetic saltation mode, the in situ measurements reproduced the HSRL measurements within 7%. Taking into account the hypothetic saltation mode, the in situ measurements overestimated the HSRL measurements by about 20%. These calculations, together with the findings that the in situ measurements were able to reproduce the direct measurements of the extinction coefficient, indicate that the presence of particles larger than measured, even at concentrations below 10^{-2} cm^{-3}, is unlikely.

5. Summary and conclusions

In our study, we have presented airborne measurements of dust layer properties, particle size distribution and mixing state of Saharan dust during SAMUM 2006.

South of the Atlas Mountains, the dust layers extended from the ground up to altitudes of about 6 km a.s.l. In contrast, over Casablanca lofted dust layers were observed at altitudes between 1 and 6 km a.s.l. The internal dust layer structure varied between well-mixed and stratified.

All dust size distributions showed a characteristic structure with two zones of different mixing state: particles in zone 1 ($D_{\mathrm{p}} < 0.5$ μm) had a non-volatile core and were coated with ammonium sulphate, whereas particles in zone 2 ($D_{\mathrm{p}} > 0.5$ μm) consisted of non-volatile components and contained light absorbing material. We evaluated the quality of the size distributions presented by comparing the extinction coefficient calculated from the in situ measurements with the direct measurements with the HSRL. In 53% of the comparisons, the deviation between HSRL extinction coefficient and calculated extinction coefficient was smaller than 15%. These intercomparisons suggest that the in situ measured size distribution is representative for the true dust size distribution.

The presence of giant particles was investigated in detail. Based on the detection limit of the FSSP-300, we defined the maximum particle size measured, $D_{\mathrm{p,\ max}}$, as the size of the particles that occurred at a concentration of 10^{-2} scm^{-3}. In all cases, particles larger than 10 μm were present, and in most cases (80%), the particles were smaller than 40 μm. In summary, $D_{\mathrm{p,\ max}}$ was between 20–40 μm for 70% of the measurements.

For the dust measured south of the Atlas Mountains, the geometric standard deviation *GSD* of the dust mode (GSD_{mode4} in Table 4) ranged between 1.42 and 2.33 with an average value of 1.72 $\pm$ 0.18. The count median diameter $CMD_{\mathrm{mode\ 4}}$ of the dust mode varied between 2.3 and 9.5 μm, with an average $CMD_{\mathrm{mode\ 4}}$ of 5.66 $\pm$ 1.48 μm. The associated average effective diameter D_{eff} is 6.5 $\pm$ 2.5 μm (6.3 $\pm$ 2.4 μm) in the dust layers south (south and north) of the Atlas Mountains. However, the dust plumes investigated revealed two main ranges of D_{eff}: the first range of D_{eff} peaked around 5 μm and the second range of D_{eff} around 8 μm. These two ranges of D_{eff} suggest that it may be inadequate to use an average effective diameter/average parametrization for a 'typical' dust size distribution. The source regions, the age and probably the mobilization mechanisms of the dust have to be considered. For these reasons, we hesitate to give a parametrization for an 'average' dust size distribution, valid for Saharan dust. Instead of giving an average dust size distribution, we have calculated the envelope for all dust size distributions measured south of the Atlas Mountains and over Casablanca (see black lines in Fig. 14). The parameters for the lower and upper envelope of all number size and surface distributions are given in Table 7 and Table 8, respectively.

The data set acquired during SAMUM 2006 will be extended by the data of the SAMUM-II field experiment, which took place in the Cape Verde area in January/February 2008. The analysis of SAMUM-II data is subject of ongoing work.

Table 7. Mode parameters of the lower and upper envelopes (black lines in top panel of Figure 14) of all airborne number size distributions measured in dust layers south of the Atlas Mountains and over Casablanca

	N_{mode1} (cm^{-3})	CMD_{mode1} (μm)	GSD_{mode1}	N_{mode2} (cm^{-3})	CMD_{mode2} (μm)	GSD_{mode2}	N_{mode3} (cm^{-3})	CMD_{mode3} (μm)	GSD_{mode3}	N_{mode4} (cm^{-3})	CMD_{mode4} (μm_	GSD_{mode4}
Upper envelope	1430	0.075	1.99	67.06	0.55	1.55	23.85	1.40	1.90	2.83	4.50	1.94
Lower envelope	425	0.070	1.74	81.97	0.20	1.41	16.39	0.50	1.85	2.09	2.00	1.80

Table 8. Mode parameters of the lower and upper envelopes (black lines in bottom panel of Figure 14) of all airborne surface distributions measured in dust layers south of the Atlas Mountains and over Casablanca

	N_{mode1} (cm^{-3})	CMD_{mode1} (μm)	GSD_{mode1}	N_{mode2} (cm^{-3})	CMD_{mode2} (μm)	GSD_{mode2}	N_{mode3} / (cm^{-3})	CMD_{mode3} (μm)	GSD_{mode3}	N_{mode4} / (cm^{-3})	CMD_{mode4} (μm)	GSD_{mode4}
Upper envelope	35	0.16	1.86	70	0.8	1.64	240	3.3	1.88	262	12	1.8
Lower envelope	6.5	0.12	1.67	9.8	0.25	1.44	21	1.12	1.88	31.5	4.4	1.78

6. Acknowledgments

We are grateful to the following participants of the SAMUM field experiment from DLR for their assistance before and during the SAMUM field phase: Reinhold Busen, Gerhard Ehret, Heinz Finkenzeller, Andreas Fix, Christian Hinz, Christoph Kiemle, Wolfgang Meier, Hans Rüba and Martin Zöger. A big 'thank you' is due to the pilots Steffen Gemsa and Stefan Grillenbeck for their perfect collaboration during SAMUM. Furthermore, we thank Jan Haßelbach and Andreas Minikin (both from DLR) for their assistance during the preparation phase for the SAMUM field experiment.

Thanks are due to Andreas Dörnbrack, Waldemar Krebs and Hermann Mannstein (all from DLR) for preparing ECMWF charts and Meteosat scenes, which formed the basis for the weather forecasts during SAMUM. We thank Yvonne Fliecker for her assistance with some of the sensitivity tests shown in Section 2.4.3.

This work was mainly funded by the German Research Foundation (Deutsche Forschungsgemeinschaft) within the project SAMUM under grant FOR 539. Significant contributions for Falcon operation from the European Space Agency under Contract No. 19429/06/NL/AR and from the European EUFAR project DARPO are gratefully acknowledged. The operation of the Falcon would also not have been possible without the full support from Royal Air Maroc, who hosted us in their facilities in Casablanca during the experiments, and from the DLR Space Programme, which contributed a significant amount to the Falcon operation budget.

References

d'Almeida, G. A. and Schütz, L. 1983. Number, mass and volume distributions of mineral aerosol and soils of the Sahara. *J. Clim. Appl. Meteorol.* **22**, 233–243.

Ansmann, A., Mattis, I., Müller, D., Wandinger, U., Radlach, M. and co-authors. 2005. Ice formation in Saharan dust over central Europe observed with temperature/humidity/aerosol Raman lidar. *J. Geophys. Res.* **110**, 1–12.

Baumgardner, D., Dye, J. E., Gandrud, B. W. and Knollenberg, R. G. 1992. Interpretation of measurements made by the forward scattering spectrometer probe (FSSP-300) during the Airborne Arctic Stratospheric Expedition. *J. Geophys. Res.* **97**, 8035–8046.

Bohren, C. F. and Huffman, D. R. 1983. *Absorption and Scattering of Light by Small Particles*. John Wiley & Sons, Inc., New York.

Borrmann, S., Luo, B. and Mishchenko, M. 2000. Application of the T-matrix method to the measurement of aspherical (ellipsoidal) particles with forward scattering optical particle counters. *J. Aerosol Sci.* **31**, 789–799.

Clarke, A. D. 1991. A thermo-optic technique for in situ analysis of size-resolved aerosol physicochemistry. *Atmos. Environ. (Part A)* **25**, 635–644.

Clarke, A. D., Shinozuka, Y., Kapustin, V. N., Howell, S., Huebert, B. and co-authors. 2004. Size distributions and mixtures of dust and black carbon aerosol in Asian outflow: physiochemistry and optical properties. *J. Geophys. Res.* **109**, D15S09.

Dubovik, O., Holben, B., Eck, T. F., Smirnov, A., Kaufman, Y. J. and co-authors. 2002. Variability of absorption and optical properties of key aerosol types observed in worldwide locations. *J. Atmos. Sci.* **59**, 590–608.

Esselborn, M., Wirth, M., Fix, A., Tesche, M. and Ehret, G. 2007. Airborne high spectral resolution lidar for measuring aerosol extinction and backscatter coefficients. *Appl. Opt.* **47**, 346–358.

Feldpausch, P., Fiebig, M., Fritzsche, L. and Petzold, A. 2006. Measurement of ultrafine aerosol size distributions by a combination of diffusion screen separators and condensation particle counters. *J. Aerosol Sci.* **37**, 577–597.

Fiebig, M. 2001. *Das troposphärische Aerosol in mittleren Breiten–Mikrophysik, Optik und Klimaantrieb am Beispiel der Feldstudie LACE 98*. Ph.D. thesis. Ludwig-Maximilians-Universität, München.

Fiebig, M., Stein, C., Schröder, F., Feldpausch, P. and Petzold, A. 2005. Inversion of data containing information on the aerosol particle size distribution using multiple instruments. *J. Aerosol Sci.* **36**, 1353–1372.

Hansen, J. E. 1971. Multiple scattering of polarized light in planetary atmospheres. Part II. Sunlight reflected by terrestrial water clouds. *J. Atmos. Sci.* **28**, 1400–1426.

Hatch, T. and Choate, S. P. 1929. Statistical description of the size properties of non uniform particulate substances. *J. Franklin Inst.* **207**, 369–387.

Hauf, T. and Clark, T. L. 1989. Three-dimensional numerical experiments on convectively forced internal gravity waves. *Q. J. R. Meteorol. Soc*. **115**, 309–333.

Haywood, J. and Boucher, O. 2000. Estimates of the direct and indirect radiative forcing due to tropospheric aerosols: a review. *Rev. Geophys.* **38**, 513–543.

Haywood, J., Francis, P., Osborne, S., Glew, M., Loeb, N., Highwood, E. and co-authors. 2003a. Radiative properties and direct radiative effect of Saharan dust measured by the C-130 aircraft during SHADE, 1: solar spectrum. *J. Geophys. Res.* **108**, 8577, doi:8510.1029/2002JD002687.

Haywood, J. M., Osborne, S. R., Francis, P. N., Keil, A., Formenti, P. and co-authors. 2003b. The mean physical and optical properties of regional haze dominated by biomass burning aerosol measured from the C-130 aircraft during SAFARI 2000. *J. Geophys. Res.* **108**, 8473, doi:8410.1029/2002JD002226.

Haywood, J. M., Allan, R. P., Culverwell, I., Slingo, T., Milton, S. and co-authors. 2005. Can desert dust explain the outgoing longwave radiation anomaly over the Sahara during July 2003? *J. Geophys. Res.* **110**, 1–14.

Heintzenberg, J. 2008. The SAMUM-1 experiment over Southern Morocco: overview and introduction. *Tellus* **61B**, doi:10.1111/j.1600-0889.2008.00403.x.

Hess, M., Koepke, P. and Schult, I. 1998. Optical properties of aerosols and clouds: the software package OPAC. *Bull. Am. Meteorol. Soc.* **79**, 831–844.

Hinds, W. C. 1999. *Aerosol Technology: Properties, Behaviour and Measurement of Airborne Particles*. John Wiley & Sons, Inc., New York.

IPCC. 2001. *Climate Change 2001: The Scientific Basis.* Cambridge University Press, Cambridge.

IPCC. 2007. *Climate Change 2007: The Scientific Basis.* Cambridge University Press, Cambridge.

Kaaden, N., Massling, A., Schladitz, A., Müller, T., Kandler, K., Schütz, L. and co-authors. 2008. State of Mixing, Shape Factor, Number Size Distribution, and Hygroscopic Growth of the Saharan Anthropogenic and Mineral Dust Aerosol at Tinfou, Morocco. *Tellus* **61B**, doi:10.1111/j.1600-0889.2008.00388.x.

Kandler, K., Schütz, L., Deutscher, C., Hofmann, H., Jäckel, S. and co-authors. 2008. Size distribution, mass concentration, chemical and mineralogical composition, and derived optical parameters of the boundary layer aerosol at Tinfou, Morocco, during SAMUM 2006. *Tellus* **61B**, doi:10.1111/j.1600-0889.2008.00385.x.

Knippertz, P., Deutscher, C., Kandler, K., Müller, T., Schulz, O. and Schütz, L. 2007. Dust mobilization due to density currents in the Atlas region: Observations from the SAMUM 2006 field campaign. *J. Geophys. Res*. **112**, D21109, doi:21110.21029/22007JD008774.

Knippertz, P., Ansmann, A., Althausen, D., Müller, D., Tesche, M. and co-authors. 2008. Dust mobilization and transport in the Northern Sahara during SAMUM 2006—a meteorological overview. *Tellus* **61B**, doi:10.1111/j.1600-0889.2008.00380.x.

Koepke, P., Hess, M., Schult, I. and Shettle, E. P. 1997. *Global Aerosol Data Set*. MPI-Report No. 243. Max-Planck-Institute for Meteorology, Hamburg, 44 pp.

Mahowald, N. M., Baker, A. R., Bergametti, G., Brooks, N., Duce, R. A. and co-authors. 2005. Atmospheric global dust cycle and iron inputs to the ocean. *Global Biogeochem. Cycles.* **19**, 1–15.

Maring, H., Savoie, D. L., Izaguirre, M. A., Custals, L. and Reid, J. S. 2003. Vertical distributions of dust and sea-salt aerosols over Puerto Rico during PRIDE measured from a light aircraft. *J. Geophys. Res.* **108**, 8587, doi:8510.1029/2002JD002544.

Miller, R. L., Tegen, I. and Perlwitz, J. 2004. Surface radiative forcing by soil dust aerosols and the hydrologic cycle. *J. Geophys. Res.* **109**, 1–24.

Moorthy, K. K., Babu, S. S., Satheesh, S. K., Srinivasan, J. and Dutt, C. B. S. 2007. Dust absorption over the "Great Indian Desert" inferred using ground-based and satellite remote sensing. *J. Geophys. Res.* **112**, D09206.

Nickovic, S., Kallos, G., Papadopoulos, A. and Kakaliagou, O. 2001. A model for prediction of desert dust cycle in the atmosphere. *J. Geophys. Res.* **106**, 18 113–18 130.

Otto, S., de Reus, M., Trautmann, T., Thomas, A., Wendisch, M. and co-authors. 2007. Atmospheric radiative effects of an in situ measured Saharan dust plume and the role of large particles. *Atmos. Chem. Phys.* **7**, 4887–4903.

Petzold, A., Rasp, K. Weinzierl, B., Esselborn, M., Hamburger, T. and co-authors. 2008. Saharan dust refractive index and optical properties from aircract-based observations during SAMUM 2006. *Tellus* **61B**, doi:10.1111/j.1600-0889.2008.00383.x.

Rasp, K, 2007. *Spektrale Absorption und Brechungsindex von Saharastaub - Ergebnisse der SAMUM-I Messkampagne*. Diploma thesis. Ludwig-Maximilians-Universität, München.

Reid, J. S., Jonsson, H. H., Maring, H. B., Smirnov, A., Savoie, D. L. and co-authors. 2003a. Comparison of size and morphological measurements of coarse mode dust particles from Africa. *J. Geophys. Res.* **108**, 8593, doi:8510.1029/2002JD002485.

Reid, J. S., Kinney, J. E., Westphal, D. L., Holben, B., Welton, E. J. and co-authors. 2003b. Analysis of measurements of Saharan dust by airborne and ground-based remote sensing methods during the Puerto Rico Dust Experiment (PRIDE). *J. Geophys. Res.* **108**, 8586, doi:8510.1029/2002JD002493.

de Reus, M., Dentener, F., Thomas, A., Borrmann, S., Stroem, J. and co-authors. 2000. Airborne observations of dust aerosol over the North Atlantic Ocean during ACE 2: Indications for heterogeneous ozone destruction. *J. Geophys. Res.* **105**, 15 263–15 275.

Rosenfeld, D., Rudich, Y. and Lahav, R. 2001. Desert dust suppressing precipitation: a possible desertification feedback loop. *PNAS* **98**, 5975–5980.

Schröder, F. and Ström, J. 1997. Aircraft measurements of sub micrometer aerosol particles (>7 nm) in the midlatitude free troposphere and tropopause region. *Atmos. Res.* **44**, 333–356.

Schütz, L. and Jaenicke, R. 1974. Particle number and mass distributions above 10^{-4}cm radius in sand and aerosol of the Sahara Desert. *J. Appl. Met.* **13**, 863–870.

Schütz, L. and Jaenicke, R. 1978. Comprehensive study of physical and chemical properties of the surface aerosols in the Cape Verde Islands region. *J. Geophys. Res.* **83**, 3585–3599.

Sokolik, I. N., Toon, O. B. and Bergstrom, R. W. 1998. Modeling the rediative characteristics of airborne mineral aerosols at infrared wavelengths. *J. Geophys. Res.* **103**, 8813–8826.

Sokolik, I. N., Winker, D. M., Bergametti, G., Gillette, D. A., Carmichael, G. and co-authors. 2001. Introduction to special section: outstanding problems in quantifying the radiative impacts of mineral dust. *J. Geophys. Res.* **106**, 18 015–18 028.

Strapp, J. W., Leaitch, W. R. and Liu, P. S. K. 1992. Hydrated and dried aerosol-size-distribution measurements from the particle measuring systems FSSP-300 probe and the deiced PCASP-100X probe. *J. Atmos. Ocean. Technol.* **9**, 548–555.

Tanré, D., Haywood, J., Pelon, J., Léon, J. F., Chatenet, B. and co-authors. 2003. Measurement and modeling of the Saharan dust radiative impact: overview of the Saharan Dust Experiment (SHADE). *J. Geophys. Res.* **108**, 8574, doi:8510.1029/2002JD003273.

Tesche, M., Ansmann, A., Müller, D., Althausen, D., Mattis, I., Heese, B. and co-authors. 2008. Vertical profiling of Saharan dust with Raman lidars and airborne high-spectral-resolution lidar during SAMUM. *Tellus* **61B**, doi:10.1111/j.1600-0889.2008.00390.x.

Toledano, C., Wiegner, M., Garhammer, M., Seefeldner, M., Gasteiger, J. and co-authors. 2008. Spectral aerosol optical depth characterization of desert dust during SAMUM 2006. *Tellus* **61B**, doi:10.1111/j.1600-0889.2008.00382.x.

Toon, O. B. and Ackerman, T. P. 1981. Algorithms for the calculation of scattering by stratified spheres. *Appl. Opt.* **20**, 3657–3660.

Veihelmann, B., Konert, M. and Van Der Zande, W. J. 2006. Size distribution of mineral aerosol: using light-scattering models in laser particle sizing. *Appl. Opt.* **45**, 6022–6029.

Virkkula, A., Ahlquist, N. C., Covert, D. S., Arnott, W. P., Sheridan, P. J. and co-authors. 2005. Modification, calibration and a field test of an instrument for measuring light absorption by particles. *Aerosol Sci. Technol.* **39**, 68–83.

Wagner, F., Bortoli, D., Pereira, S., Costa, M., Silva, A. M. and co-authors. 2008. Properties of dust aerosol particles transported to Portugal from the Sahara desert. *Tellus* **61B**, doi:10.1111/j.1600-0889.2008.00393.x.

Wiegner, M., Gasteiger, J., Kandler, K., Weinzierl, B., Rasp, K. and co-authors. 2008. Numerical simulations of optical properties of Saharan dust aerosols with emphasis on lidar applications. *Tellus* **61B**, doi:10.1111/j.1600-0889.2008.00381.x.